

# Strain-release alkylation of Asp12 enables mutant selective targeting of K-Ras-G12D

Received: 21 August 2023

Accepted: 30 January 2024

Published online: 05 March 2024

 Check for updatesQinheng Zheng<sup>1,3</sup>, Ziyang Zhang<sup>1,2,3</sup>✉, Keelan Z. Guiley<sup>1</sup> & Kevan M. Shokat<sup>1,2</sup>✉

K-Ras is the most commonly mutated oncogene in human cancer. The recently approved non-small cell lung cancer drugs sotorasib and adagrasib covalently capture an acquired cysteine in K-Ras-G12C mutation and lock it in a signaling-incompetent state. However, covalent inhibition of G12D, the most frequent K-Ras mutation particularly prevalent in pancreatic ductal adenocarcinoma, has remained elusive due to the lack of aspartate-targeting chemistry. Here we present a set of malolactone-based electrophiles that exploit ring strain to crosslink K-Ras-G12D at the mutant aspartate to form stable covalent complexes. Structural insights from X-ray crystallography and exploitation of the stereoelectronic requirements for attack of the electrophile allowed development of a substituted malolactone that resisted attack by aqueous buffer but rapidly crosslinked with the aspartate-12 of K-Ras in both GDP and GTP state. The GTP-state targeting allowed effective suppression of downstream signaling, and selective inhibition of K-Ras-G12D-driven cancer cell proliferation in vitro and xenograft growth in mice.

Oncogenic mutations of Ras are among the most common genetic alterations in human cancer, with an estimated disease burden of >3 million new patients per year worldwide<sup>1</sup>. Despite widespread appreciation of the importance of Ras in cancer, direct binding ligands that block downstream signaling were not reported until 2013 (ref. 2) due to the lack of obvious drug-binding pockets in the protein. The only clinically approved K-Ras inhibitors are completely mutant specific as they rely on covalent recognition of the highly nucleophilic somatic cysteine residue of K-Ras-G12C. Recent preclinical reports<sup>3,4</sup> of non-covalent K-Ras binding inhibitors have emerged that lack exclusive mutant specificity and exhibit varying degrees of biochemical preference for mutant K-Ras over the wild type. The challenge in covalent targeting the most common single variant in K-Ras-driven tumors (G12D) is that the carboxylic acid side chains of Asp and Glu are among the least nucleophilic heteroatom containing amino acid (a.a.) side chains. A further challenge for electrophiles capable of reacting with weak nucleophiles (Asp/Glu) is the need to withstand 55 M water and hypernucleophiles such as glutathione (GSH) in biological buffers.

No suitable electrophiles for selectively targeting acidic a.a. side chains in aspartic or glutamic acids at physiological pH have been reported<sup>5–8</sup> despite advances<sup>9</sup> in targeting neutral or basic ones such as lysine<sup>10–12</sup>, tyrosine<sup>13</sup>, serine<sup>14,15</sup>, arginine<sup>16</sup>, methionine<sup>17</sup> and histidine<sup>18–20</sup>. In this Article, we report an electrophile that alkylates the mutant aspartate in K-Ras-G12D in both GDP- and GTP-bound states, blocks effector interactions and inhibits the growth of K-Ras-G12D-driven cell lines.

## Results

### A malolactone covalently modifies mutant Aps12

To covalently target the mutant aspartate, we focused on electrophiles designed to exploit strain release upon carboxylate attack of small three- and four-membered heterocyclic ring systems. Our<sup>21</sup> and others<sup>22</sup> exploration of electrophiles from the literature showed modest levels of K-Ras-G12D crosslinking exhibited by three-membered rings—*NH*-aziridine and epoxide electrophiles covalently modified K-Ras-G12D by 40–60% over the course of 24 h (Extended Data Fig. 1a,b). Further optimization proved unsuccessful due to the limited

<sup>1</sup>Department of Cellular and Molecular Pharmacology, Howard Hughes Medical Institute, University of California, San Francisco, CA, USA. <sup>2</sup>Department of Chemistry, University of California, Berkeley, CA, USA. <sup>3</sup>These authors contributed equally to this work: Qinheng Zheng, Ziyang Zhang.

✉ e-mail: [ziyang@berkeley.edu](mailto:ziyang@berkeley.edu); [kevan.shokat@ucsf.edu](mailto:kevan.shokat@ucsf.edu)

number of chemically stable modifications possible in three-membered rings. A recent report<sup>23</sup> demonstrated that structurally similar epoxides could label recombinant K-Ras-G12D at extremely high concentration (1 mM), which precluded its use as a targeted covalent inhibitor in cells. A covalent K-Ras-G12D inhibitor based on cyclophilin recruitment has been reported in a meeting abstract<sup>8</sup>.

The four-membered ring electrophile  $\beta$ -lactone, found in both natural products and synthetic drugs<sup>14,24,25</sup>, was attractive because the parent  $\beta$ -propiolactone, a potent acylating and alkylating reagent<sup>26–32</sup>, modified K-Ras-G12D at multiple sites including the target Asp12 residue (Extended Data Fig. 2a) in a dose-dependent manner (Extended Data Fig. 2b). However, the [4.2.0]-fused  $\beta$ -lactones that covalently acylated a sibling K-Ras-G12S mutation<sup>14</sup> were not reactive with G12D (Supplementary Fig. 1a), requiring exploration of another means to activate the nucleophilic attack of the  $\beta$ -lactone by Asp12.

Ambident electrophile  $\beta$ -lactones react with carboxylates with a preference at the  $\beta$ -carbon via an alkylation pathway at the  $\beta$ -carbon<sup>25,33</sup> (cf. alcohols such as the serine side chain prefer acylation via carbonyl attack). The alkylation trajectory in the [4.2.0]-fused  $\beta$ -lactones at the bridgehead carbon was not accessible to Codon12 side chains (Supplementary Fig. 1b). We reasoned that switching the fused ring system to a simple carbonyl bridge would (1) geometrically enable the  $\beta$ -lactone electrophile to be poised for  $S_N2$  attack from the P-Loop Asp12, (2) activate the alkylation pathway by carbonyl  $\pi^*$ -orbital participation and (3) potentially provide further hydrogen bonding activation by the neighboring Lys16 shown to be important in activating of K-Ras-G12C acrylamide electrophiles<sup>34</sup>.

A series of recently reported high-affinity noncovalent small molecules<sup>35,36</sup>, including MRTX1133 (refs. 3,37), which binds to K-Ras-G12D and wild-type (WT) K-Ras<sup>38</sup> provided the necessary scaffold for presenting the electrophilic fragment toward the Asp12. We prepared (*RS*)-G12Di-1 (**1**) as a racemate by coupling ( $\pm$ )- $\beta$ -carboxyl- $\beta$ -propiolactone, also known as malolactone, to the bicyclic piperazine group of a Switch-II Pocket (S-IIP) ligand scaffold using the carbonyl bridge design (Fig. 1a). Using whole-protein mass spectrometry (MS), we assessed the reactions between recombinant K-Ras proteins and 10  $\mu$ M (*RS*)-G12Di-1 at 23 °C (Fig. 1b,c). (*RS*)-G12Di-1 reacted rapidly with K-Ras-G12D•GDP with a half-life of 99 s (95% confidence interval 83–118 s) and fully modified K-Ras-G12D•GDP in less than 15 min (Fig. 1d). By contrast, (*RS*)-G12Di-1 achieved only  $6.5 \pm 0.3\%$  modification of K-Ras-G13D•GDP and no detectable modification of K-Ras-WT•GDP after 1 h. Interestingly, (*RS*)-G12Di-1 showed markedly reduced reactivity with K-Ras-G12E•GDP, a nonnatural mutant that positions its carboxylate nucleophile (Glu) further from the backbone than that in G12D, and K-Ras-G12S•GDP. Although less potent, (*RS*)-G12Di-1 was also active against the GppNHP-bound K-Ras-G12D. This is distinct from S-IIP K-Ras-G12C inhibitors, which exclusively recognize the GDP-bound state<sup>2,34,39–42</sup>, whereas GTP-state recognition has so far only been observed for compounds with a different binding mechanism<sup>8,43</sup>. A recently reported K-Ras-G12C inhibitor dependent on cyclophilin recruitment is capable of GTP-state recognition and showed faster in-cell signaling inhibition kinetics<sup>43</sup>. The covalent modification of Asp12 by (*RS*)-G12Di-1 stabilized both K-Ras-G12D•GDP and K-Ras-G12D•GppNHP toward thermal denaturation ( $\Delta T_m = +10.3$  °C and  $+2.5$  °C, respectively). The adduct between K-Ras-G12D and (*RS*)-G12Di-1 was stable over pH 4.5–7.5, and did not degrade in the presence of 1 vol% of dithiothreitol (DTT) or hydrazine at 23 °C showing its intrinsic resistance to nucleophiles in the bulk solution (Extended Data Fig. 3).

The ability of (*RS*)-G12Di-1 to engage the GppNHP-bound state of K-Ras-G12D prompted us to ask whether such a covalent modification could disrupt the interaction with effector proteins such as Raf. Using a time-resolved fluorescence energy transfer assay<sup>44</sup>, we found that (*RS*)-G12Di-1 inhibited the interaction between Raf-RBD and K-Ras-G12D, but not WT K-Ras, in a dose-dependent fashion (Fig. 1e).

We also measured the interaction between immobilized Raf-RBD with fully labeled K-Ras-G12D•GppNHP•(*RS*)-G12Di-1 using biolayer interferometry. Compared to unmodified K-Ras-G12D•GppNHP, the K-Ras-G12D•GppNHP•(*RS*)-G12Di-1 complex showed substantially decreased binding to Raf-RBD (Fig. 1f). Such a feature may be particularly advantageous for the G12D mutant, as its severely impaired GTP hydrolysis<sup>45</sup> renders an abundant and persistent K-Ras population in the active GTP-state in the cell.

### Mechanism- and structure-guided ligand evolution

To better understand the covalent reaction in the S-IIP of KRAS (G12D) between (*RS*)-G12Di-1 and Asp12, we solved a 1.7-Å crystal structure of the K-Ras-G12D•GDP•(*RS*)-G12Di-1 adduct (Fig. 1g). We observed (*RS*)-G12Di-1 in the S-IIP pocket adopting a conformation similar to that seen for K-Ras-G12C inhibitors (Supplementary Fig. 2), with clear electron density for the covalent ester bond between Asp12 and the compound as well as the free carboxyl group resulting from the ring opening. This high-resolution structure also allowed us to assign the stereochemistry of the adduct as *S* at the  $\beta$ -carbon (Fig. 1h,i). Because we obtained the co-crystal using racemic (*RS*)-G12Di-1, this *S* stereochemistry could in theory result from an  $S_N2$  attack on the  $\beta$ -carbon of *R* enantiomer of G12Di-1 or an attack on the carbonyl of the *S* enantiomer of G12Di-1 followed by an acyl transfer (Extended Data Fig. 4a). To distinguish between these two possibilities, we prepared pure *R* and *S* enantiomers of a structural analog. Monitoring the reaction rate with K-Ras-G12D•GDP showed that the *R* enantiomer (*R*)-G12Di-2 (**2**) was significantly more reactive toward K-Ras-G12D•GDP (Extended Data Fig. 4b). Furthermore, we observed the same *R*  $\gg$  *S*  $C_\alpha$ -enantioselectivity (that is,  $C_2$  in malolactone system) in the context of K-Ras-G12D labeling across a panel of strain-release electrophiles such as epoxides and aziridines that can only react via an  $S_N2$  mechanism (Extended Data Fig. 1). Such enantioselectivity favoring a direct  $S_N2$  ring-opening mechanism aligns with literature observations with  $\beta$ -lactones<sup>25,33</sup>. The predominant  $S_N2$  preference of ring-opening reaction by Asp12 is distinct from the preference for attack by water, that is, hydrolysis, which often takes place at the carbonyl in near-neutral buffers<sup>46</sup>.

Despite being a potent covalent ligand of recombinant K-Ras-G12D, (*RS*)-G12Di-1 was not stable in aqueous buffers at pH 7.4, precluding its use in cellular assays. We reasoned that its stability could be improved by attaching substituents at either or both sides of the  $\alpha$ -carbon. Substitutions at the  $\alpha$ -carbon will block the trajectory of incoming water nucleophiles from at least one side of the  $\beta$ -lactone ring (Fig. 2a, lower path). The same modification of the electrophile was predicted to have little impact on the  $S_N2$  attack by Asp12 because of the pseudo-staggered conformation of the lowest unoccupied molecular orbital of the C–O bond and the  $\alpha$ -carbon steric hindrance (Fig. 2a, upper path).

To test this hypothesis, we prepared (*2R,3S*)-G12Di-3 (**3**) and (*2R,3S*)-G12Di-4 (**4**) with increasing steric hinderance at the pro-*S* position of the  $\alpha$ -carbon ( $C_3$  in Fig. 2b). G12Di-2–4 maintained the ability to react with K-Ras-G12D, although the bulkier compounds exhibited decreased reaction rates (Fig. 2c). Meanwhile, (*2R,3S*)-G12Di-4, bearing an isopropyl group, resisted hydrolysis, with >90% of the material remaining intact after 24 h at 23 °C and pH 7.4. By contrast, (*R*)-G12Di-2 and (*2R,3S*)-G12Di-3 exhibited half-lives of 1.7 h and 2.5 h, respectively (Fig. 2d).

With an improved isopropyl (*i*-Pr)-substituted malolactone electrophile, we further explored S-IIP ligands with higher affinity, including the 8-ethynyl naphthyl ligand in (*RS*)-G12Di-1 ((*2R,3S*)-G12Di-5 (**5**)) and MRTX1133 ((*2R,3S*)-G12Di-6 (**6**))<sup>35–37</sup>. The fast kinetics of GDP-state labeling persisted, (*2R,3S*)-G12Di-5 and (*2R,3S*)-G12Di-6 labeled the GTP-state up to 200-fold faster than (*2R,3S*)-G12Di-4, possibly due to the accessibility of the S-IIP of K-Ras-G12D•GTP to the MRTX1133 scaffold. When tested at 10  $\mu$ M, compound (*2R,3S*)-G12Di-6 fully labeled 200 nM (ref. 47) of K-Ras-G12D•GppNHP within 5 min, which

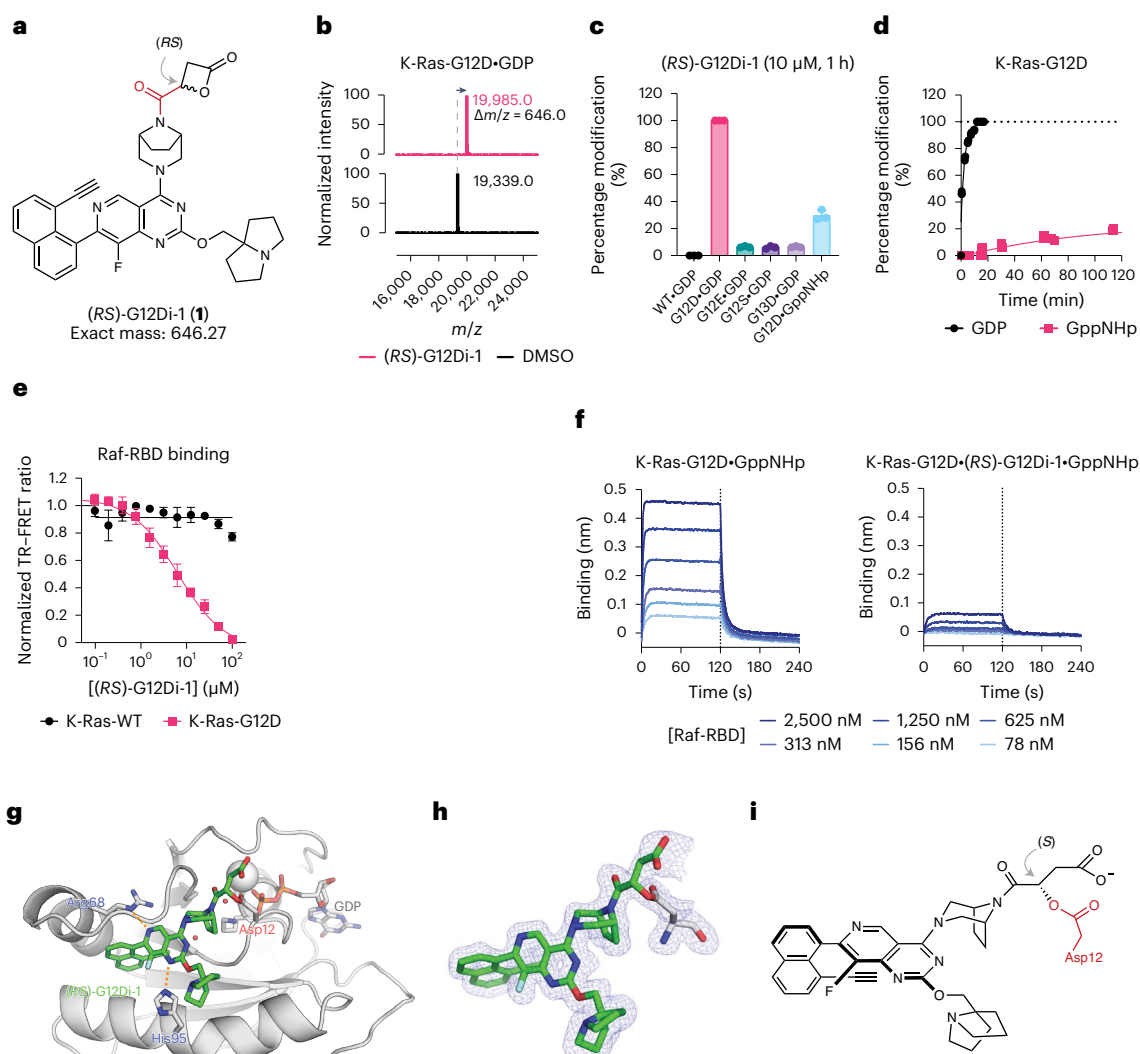


**Fig. 1 | Malolactone (RS)-G12Di-1 (1) is a selective, covalent inhibitor of K-Ras-G12D.** **a**, Chemical structure of racemic (RS)-G12Di-1. **b**, Deconvoluted protein mass spectra of Cyslight K-Ras-G12D•GDP in the presence or absence of (RS)-G12Di-1. Mass spectra are representative of two independent experiments. **c**, Compound (RS)-G12Di-1 selectively labeled K-Ras-G12D not WT or other mutants. All data points represent individual biological replicates. Data are presented as mean  $\pm$  standard deviation ( $n = 3$ ). **d**, Kinetics of K-Ras-G12D (200 nM) labeling with (RS)-G12Di-1 (10  $\mu$ M) ( $n = 3$ , replicates are plotted as individual

data points). **e**, Time-resolved fluorescence energy transfer dose–response of (RS)-G12Di-1 induced Ras-Raf•RBD binding disruption. All data points represent individual biological replicates. Data are presented as mean  $\pm$  standard deviation ( $n = 3$ ). **f**, Biolayer interferometry dose–response of GST-Raf•RBD binding with K-Ras-G12D•GppNHp without or with covalently labeled (RS)-G12Di-1. **g**, Co-crystal structure of K-Ras-G12D•GDP•(RS)-G12Di-1. **h**,  $2F_o - F_c$  map for the covalently bound ligand (RS)-G12Di-1 and Asp12 is depicted in blue mesh (1.0 $\sigma$ ). **i**, Chemical structure of covalently bound ligand with the configuration of  $\beta$ -carbon assigned as S.

is, to our knowledge, the first S-IIP covalent molecule that has a preference for GTP state of K-Ras (Fig. 3b). Unlike MRTX1133, which prefers the GDP state<sup>48</sup>, its (2*R*,3*S*)-3-isopropyl malolactone derivative (2*R*,3*S*)-G12Di-6 preferred the GTP state as assessed by intact protein MS. The in-cell K-Ras-G12D covalent labeling kinetics using a western blot time course mirrored the recombinant protein results (Fig. 3c), where (2*R*,3*S*)-G12Di-6 labeled endogenous K-Ras-G12D completely in homozygous *KRAS*<sup>G12D/G12D</sup> cancer cell line SW1990 within 2 h as indicated by the gel mobility shift in the anti-Ras immunoblot, and concomitant reduction of the phospho-ERK levels. This is consistent with the higher biochemical potency we observed with K-Ras-G12D•GppNHp, as cellular K-Ras-G12D is enriched in the GTP-bound state as a result of its poor intrinsic and GAP mediated GTPase activity<sup>45</sup>.

To understand the significantly improved GTP-state labeling kinetics from (2*R*,3*S*)-G12Di-5 to (2*R*,3*S*)-G12Di-6, we synthesized six compounds ((2*R*,3*S*)-G12Di-5a (7) to (2*R*,3*S*)-G12Di-5f (12), Fig. 3d) exploiting their difference in the S-IIP binding core substitution pattern. Measuring the pseudo-first-order kinetic rates with 200 nM

K-Ras-G12D and 10  $\mu$ M compounds, GTP-state labeling was more sensitive to these substitution changes with higher coefficient of variation ( $CV_{\text{GppNHp}}$  1.1,  $CV_{\text{GDP}}$  0.5). We grouped compounds with or without certain substitution, and analyzed the means of pseudo-first-order rates using Student's *t*-test (Fig. 3e). While the two fluorine substitutions on the naphthyl ring or the bicyclic tertiary amine were dispensable, naphthyl 3-OH substitution was critical for fast GTP-state covalent labeling ( $P = 0.0019$ ). Besides the gain of GTP-state labeling kinetics, the 3-hydroxy in the naphthyl ring significantly stabilized the covalent complex by 5–9  $^{\circ}\text{C}$  ( $\Delta\Delta T_m$ , 3-hydroxy group versus 3-hydrogen, Supplementary Table 6). We reason that the hydrogen bonding (2.7  $\text{\AA}$ , as measured in Protein Data Bank (PDB) access code 7T47) between naphthyl 3-OH and Asp69 side chain is critical for S-IIP inhibitors to access the GTP state and stabilize the complex. Similar interaction exists in previous GTP-state-selective cyclic peptide KD2 (ref. 44) and K-Ras-G12C inhibitors ARS-853 and ARS-107 (ref. 34), highlighting an underappreciated pharmacophore for active state targeting of K-Ras.

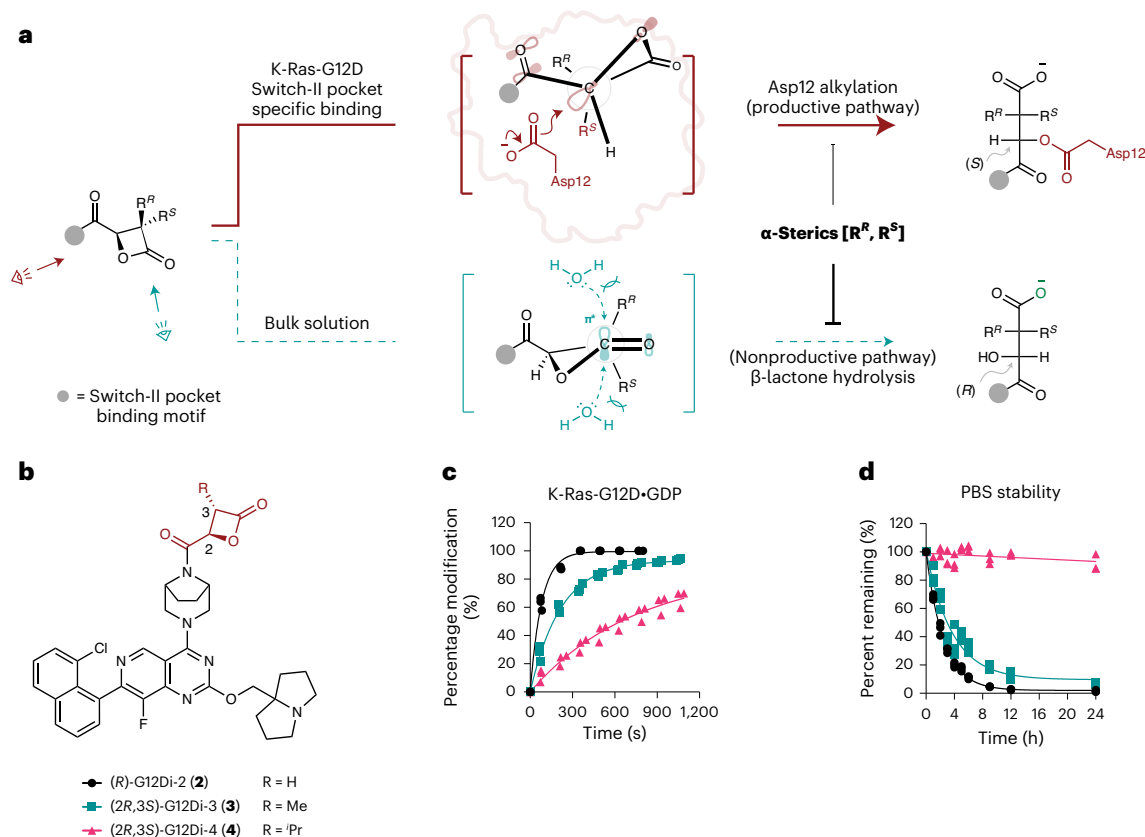


**Fig. 2 | Sterically hindered  $\beta$ -lactones are stable and potent inhibitors of K-Ras-G12D.** **a**, Mechanistic analysis of the Asp12-alkylating (red) and hydrolytic (teal) processes reveals the higher sensitivity of the latter to C3 substituents. **b**, Chemical structures of C3-substituted malolactones (R)-G12Di-2 (**2**), (2R,3S)-

G12Di-3 (**3**), and (2R,3S)-G12Di-4 (**4**). **c**, Recombinant K-Ras-G12D (200 nM) labeling kinetics with 3-substituted malolactones (10  $\mu$ M) ( $n = 3$ , replicates are plotted as individual data points). **d**, Stability of 3-substituted  $\beta$ -lactones in PBS (pH 7.4) by LC-MS ( $n = 3$ , replicates are plotted as individual data points).

### Optimized ligand inhibits tumor growth in vitro and in vivo

Despite efficient labeling of K-Ras-G12D by G12Di-4–6 in cells, these compounds did not show significant mutant selectivity in terms of cell growth inhibition in a survey of seven cancer cell lines including three *KRAS*<sup>G12D</sup> mutant lines and four with either WT *KRAS* or non-G12D *KRAS* mutations (Extended Data Fig. 5a,b). We reasoned that G12Di-4–6 may possess cellular targets that are critical for cell survival other than K-Ras-G12D. We ruled out inhibition of WT K-Ras based on the effect on A375 cells that possess a downstream BRAF (V600E) activating mutation that should bypass K-Ras-WT inhibition. We next turned to the monosubstituted malolactone electrophile in G12Di-4–6, which resembles that found in the natural product belactosin C (refs. 49–51), a potent covalent inhibitor of the eukaryotic proteasome (Extended Data Fig. 6). We confirmed that compounds G12Di-4–6 inhibited proteasome activity and induced accumulation of poly-ubiquitinated proteins in HEK293 cells (Extended Data Fig. 6). Because proteasome inhibition leads to cell growth inhibition independent of K-Ras-G12D mutation, we sought to eliminate this off-target activity.

Through comparison of the co-crystal structure of a belactosin C derivative bound to the yeast proteasome (PDB: 3TDD) and that of (R)-G12Di-1 bound to K-Ras-G12D•GDP, we hypothesized that introduction of a second substitution at the pro-R position would block proteasome binding and further improve hydrolytic stability (Extended Data Fig. 7). Based on this design approach, we also reasoned that the larger pro-S isopropyl substitution introduced previously would not be required if both hydrogens were substituted and therefore designed a 3,3-gem-dimethyl substituted malolactone, (R)-G12Di-7 (**13**). As predicted, (R)-G12Di-7 with a doubly substituted electrophile showed excellent stability ( $t_{1/2} > 24$  h) in the presence of reduced GSH in phosphate-buffered saline (PBS) at 37 °C for 24 h (Extended Data Fig. 8).

(R)-G12Di-7 did not inhibit proteasome activity or induce protein poly-ubiquitination in HEK293 cells (Extended Data Fig. 6). We further show that (R)-G12Di-7 was highly selective for K-Ras-G12D and did not induce more than 20% inhibition in a panel of 482 kinases commonly used in safety profiling (Supplementary Table 10). (R)-G12Di-7 completely labeled K-Ras-G12D•GDP and K-Ras-G12D•GppNHp within 30 min and 300 min, respectively (Fig. 4b). The slower GppNHp-state labeling kinetics (cf. (2R,3S)-G12Di-6) was mainly due to the electrophile's lower intrinsic reactivity ( $k_{\text{inact}}$ ) (Supplementary Table 5). (R)-G12Di-7 showed high mutant selectivity, labeling only the GDP and GppNHp state of G12D, but not the GDP state of WT, G12E, G12S or G13D despite elongated incubation time (Fig. 4d). The most reactive G12C mutant was also covalently labeled by (R)-G12Di-7. (R)-G12Di-7 stabilized both GDP and GppNHp-bound K-Ras-G12D by 18.6 °C and 11.7 °C, respectively (Extended Data Fig. 9).

The mutant-selective, in-cell covalent labeling was assessed by immunoblots, where (R)-G12Di-7 labeled endogenous K-Ras-G12D completely in homozygous *KRAS*<sup>G12D/G12D</sup> cell lines SW1990 and AsPC-1, only half in the heterozygous *KRAS*<sup>G12D/WT</sup> AGS cell line, and none in non-G12D mutation cell lines (Fig. 4e). The mutant selectivity was consistent between in-cell covalent modification and downstream signaling suppression. By contrast, the reversible inhibitor MRTX1133 is reported to inhibit WT *KRAS* signaling at concentrations >100 nM in mouse embryonic fibroblasts (MEF) cells engineered to express one single *RAS* allele ('Rasless MEFs')<sup>38</sup>. Washout experiment demonstrated the stability of the covalent K-Ras-G12D•(R)-G12Di-7 complex in cells over a course of 12 h (Fig. 4f).

To examine the on-target inhibition, we used *KRAS*<sup>G12D</sup>-transformed mouse pro-B cell line Ba/F3. The parental Ba/F3 cell line is dependent on interleukin 3 (IL-3) for survival and proliferation, while the transformed

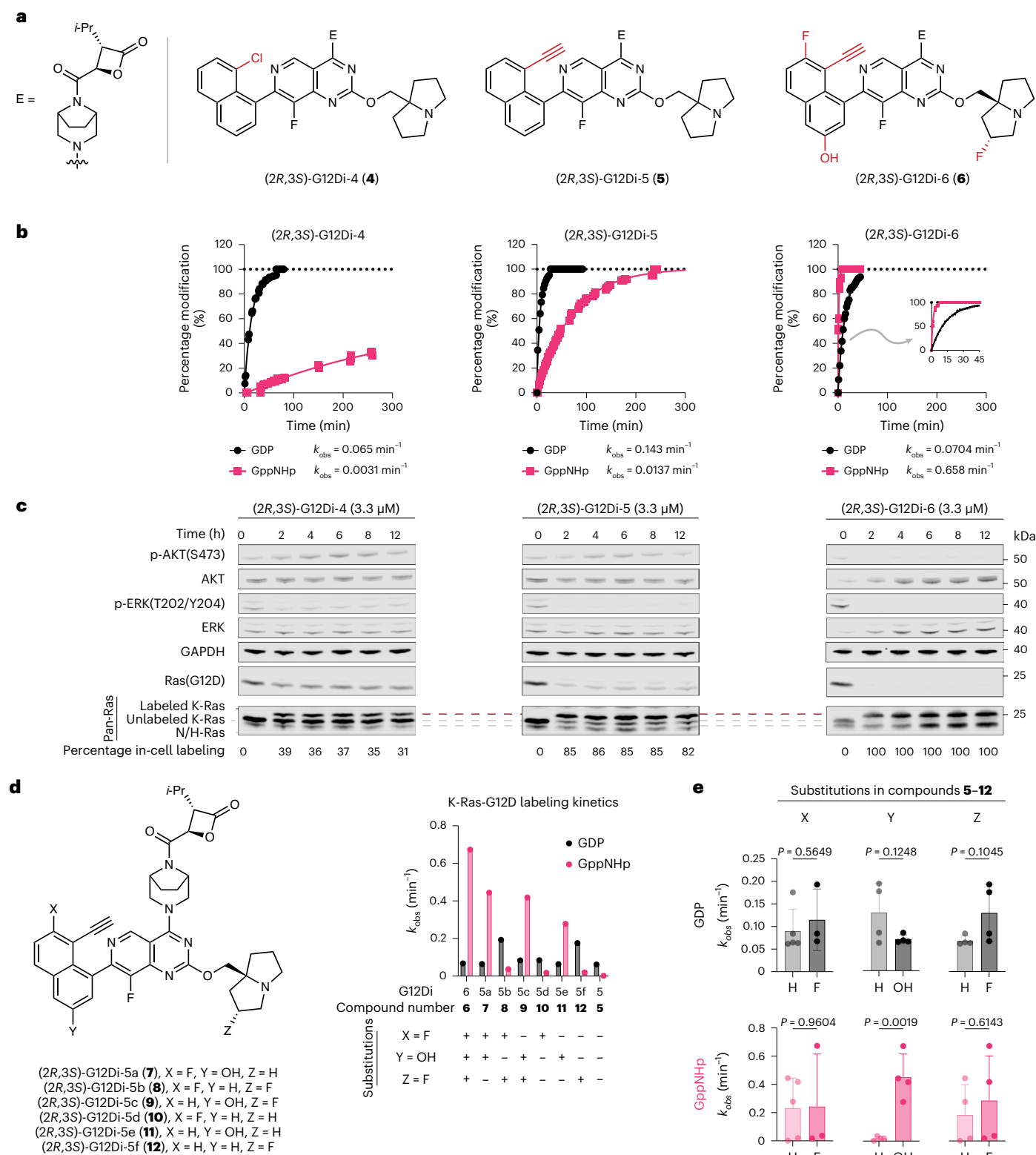


**Fig. 3 | Rapid covalent modification of K-Ras-G12D-GTP is essential for in-cell target engagement and oncogenic signaling suppression. a**, Chemical structures of (2R,3S)-G12Di-4 (**4**), (2R,3S)-G12Di-5 (**5**) and (2R,3S)-G12Di-6 (**6**). **b**, Recombinant K-Ras-G12D (200 nM) labeling kinetics with 3-isopropyl malolactones (10  $\mu\text{M}$ ) ( $n = 3$ , replicates are plotted as individual data points). **c**, Western blot time course of cellular K-Ras-G12D covalent engagement and downstream signaling inhibition. Data are representative of two independent

experiments. **d**, Covalent K-Ras-G12D labeling kinetics in both nucleotides by (2R,3S)-G12Di-5, (2R,3S)-G12Di-6 and (2R,3S)-G12Di-5a–5f (**7–12**). Substitutions X, Y and Z vary between compounds **7–12**. **e**, Analysis of the determining substitution on covalent labeling kinetics by an unpaired *t*-test comparing X = H ( $n = 5$ ) or F ( $n = 3$ ), Y = H ( $n = 4$ ) or OH ( $n = 4$ ), and Z = H ( $n = 4$ ) or F ( $n = 4$ ). All data points represent individual chemical compound. Data are presented as mean  $\pm$  standard deviation.

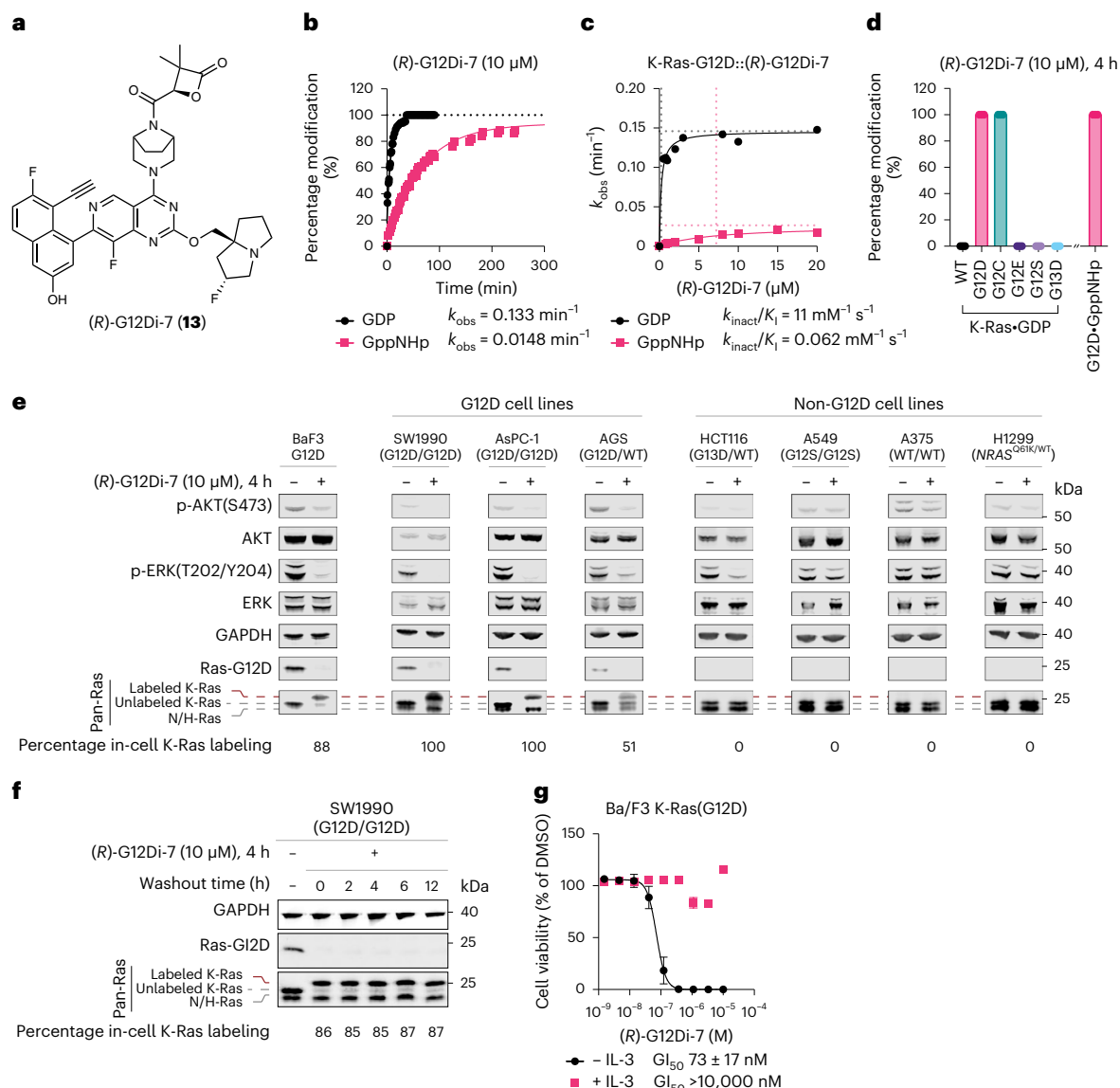


**Fig. 4 | Malolactone (R)-G12Di-7 (13) covalently and mutant-selectively modified recombinant and endogenous K-Ras-G12D oncoprotein in cancer cell lines.** **a**, Chemical structure of (R)-G12Di-7. **b**, Pseudo-first-order K-Ras-G12D labeling kinetics of (R)-G12Di-7. Conditions: K-Ras-G12D (200 nM), (R)-G12Di-7 (10 μM), room temperature. **c**, Second-order K-Ras-G12D labeling kinetics of (R)-G12Di-7. **d**, Covalent labeling selectivity against K-Ras WT and mutants. All data points represent individual biological replicates. Data are presented as mean  $\pm$  standard deviation ( $n = 3$ ). **e**, Immunoblot of Ba/F3:K-Ras-G12D, SW1990

AsPC-1, AGS, HCT116, A549, A375 and H1299 cells treated with DMSO or 10 μM (R)-G12Di-7 for 4 h. Data are representative of two independent experiments. **f**, Stability of covalent complex G12D\*(R)-G12Di-7 in cells. Data are representative of two independent experiments. **g**, Relative growth of Ba/F3:K-Ras-G12D cells (with or without 10 ng ml<sup>-1</sup> IL-3) after treatment with (R)-G12Di-7 for 72 h. Data are presented as mean  $\pm$  standard deviation ( $n = 3$ ) and are representative of two independent experiments.

cells become independent of IL-3 but dependent on the transduced driver oncogene<sup>52</sup>. (R)-G12Di-7 inhibited growth of Ba/F3(KRAS<sup>G12D</sup>) cells with a GI<sub>50</sub> of 73  $\pm$  17 nM. The same cells co-treated with IL-3 (10 ng ml<sup>-1</sup>) lost sensitivity to (R)-G12Di-7 up to 10 μM suggesting the observed cell growth inhibition was due to on-target K-Ras-G12D inhibition (Fig. 4g).

This compound further showed significantly biased inhibition profile toward K-Ras-G12D mutation (SW1990, AsPC-1 and AGS) from non-G12D mutation cancer cell lines (H1299, HCT116, A549 and A375) in 2D-adherent monolayer cultures. (R)-G12Di-7 showed minimal toxicity to the latter cell lines at concentrations up to 10 μM. Similar cell growth inhibition potency as well as selectivity was observed in 3D-spheroid suspensions<sup>39</sup> (Fig. 5a). The cellular activity of (R)-G12Di-7 could be translated to a K-Ras-G12D cell line-derived xenograft in mice. We observed a dose-dependent inhibition of SW1990 xenograft growth as measured by volume upon treatment of (R)-G12Di-7 over a course

of 28 days (Fig. 5b). No apparent toxicity induced by compound treatment was evidenced by the comparable weight gain over the treatment period in both groups of mice.

Further, we demonstrated the importance of covalency by testing three noncovalent analogs of our lead molecule (R)-G12Di-7, including its hydrolyzed product and two nonlactone cyclic analogs, β-lactam and cyclobutanone (Extended Data Fig. 10). The noncovalent analogs with amide pendants demonstrated moderate (>1 μM) GI<sub>50</sub> values against K-Ras-G12D cell lines. Coupled with a covalent bond formation event in (R)-G12Di-7, the S-IIP engagement was significantly augmented leading to submicromolar GI<sub>50</sub> values for K-Ras-G12D mutation cells and higher mutant selectivity. These results suggested that strong reversible S-IIP engagement, well-tuned G12D reactivity and hydrolytic stability are critical for achieving potent and selective cellular inhibition.

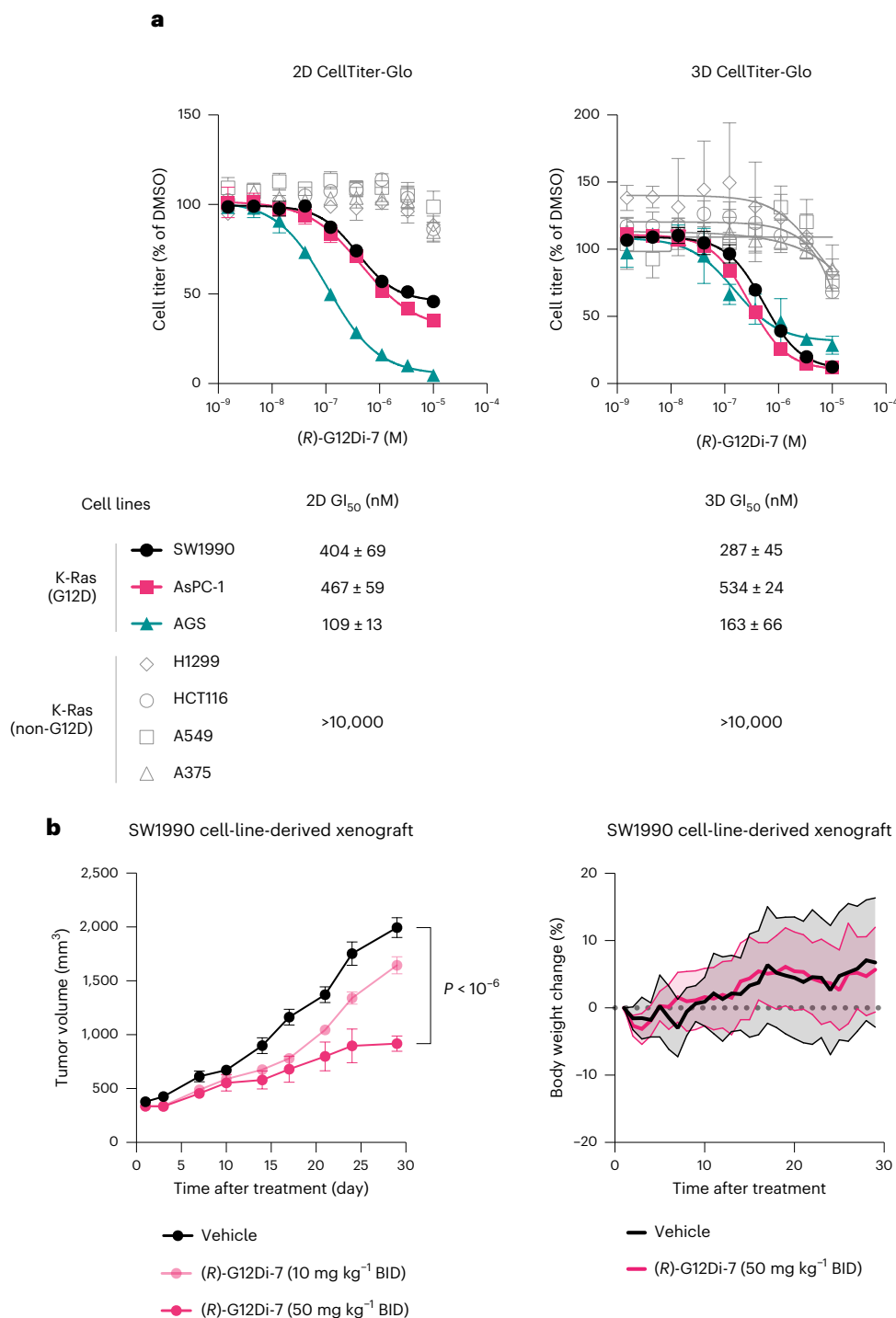


**Fig. 5 | Covalent K-Ras-G12D inhibitor (R)-G12Di-7 selectively inhibits cell growth in cancer cell lines harboring *KRAS*<sup>G12D</sup> mutation and tumor growth in mice bearing SW1990 xenograft. a**, Relative growth of cancer cell lines with (black, red or teal) or without (gray) *KRAS*<sup>G12D</sup> mutation after treatment with (R)-G12Di-7 for 72 h (2D) or 120 h (3D). Data are presented as mean ± standard deviation ( $n = 3$ ) and are representative of two independent experiments. **b**, Tumor volumes and body weight of mice bearing SW1990 xenografts and

treated with vehicle (10% captisol in 1× PBS,  $n = 8$  biologically independent mice), (R)-G12Di-7 (10 mg kg<sup>-1</sup>,  $n = 9$  biologically independent mice), or (R)-G12Di-7 (50 mg kg<sup>-1</sup>,  $n = 9$  biologically independent mice). BID, twice a day. All data points represent individual biological replicates. Data are presented as mean ± standard error of the mean. Tumor volumes for the (R)-G12Di-7 (50 mg kg<sup>-1</sup>) treatment groups are statistically significant versus vehicle ( $P < 0.00001$ ) by two-tailed Student's *t*-test.

## Discussion

The discovery that the mutant cysteine in K-Ras-G12C can be exploited by small-molecule electrophiles has opened a new way to target oncogenic K-Ras-driven cancers. This has led to the recent US Food and Drug Administration approval of sotorasib and adagrasib. However, the much larger patient population bearing an acquired aspartic acid missense

mutation at the same K-Ras Gly12 position remains a significant therapeutic challenge at the forefront of current research. This is partially due to the significantly lower nucleophilicity of aspartate compared to that of cysteine in aqueous solution<sup>2,53,54</sup>. The malolactone ligands described here efficiently covalently modify the mutant aspartate in K-Ras (G12D) in both the GDP- and GTP-bound states. The GDP/GTP

dual state inhibitors hold the potential to provide desirable pharmacodynamics compared to inactive-state K-Ras inhibitors. One particular malolactone example ((2*R*,3*S*)-G12Di-6) predominantly labeled the GTP-bound state in K-Ras-G12D compared to the GDP state, leading to faster in-cell covalent modification and signaling pathway suppression (Fig. 3c). We further uncovered a critical hydrogen bonding interaction between S-IIP ligands and K-Ras Asp69 that contributes to the GTP-state engagement. It will be interesting to further explore the molecular determinants of GTP-state-preferring ligands especially in the context of pan-KRAS<sup>4</sup> reversible ligands as this approach may provide some measure of WT-sparing activity since the GDP state predominates in the WT compared to the oncogenic mutants.

Although it is believed that the liable ester linkages are readily cleaved in the cytosolic environment<sup>55</sup>, time course immunoblots suggested that the K-Ras-G12D•malolactone complex remains intact for at least 12 h. Our observation suggests that ester bonds protected by the protein host in the ligand-binding pocket may be more resistant to intrinsic or esterase-mediated hydrolysis, a feature that could be exploited in the development of carboxylate-targeting covalent ligands beyond K-Ras-G12D inhibitors.

Together, our data demonstrate that strain release can be exploited to trap a common somatically mutated aspartate residue on the surface of the oncogene K-Ras-G12D. Compound (*R*)-G12Di-7 is a covalent ligand of K-Ras-G12D with potent and mutant-selective activity against K-Ras-G12D cancers in vitro and in vivo.

## Online content

Any methods, additional references, Nature Portfolio reporting summaries, source data, extended data, supplementary information, acknowledgements, peer review information; details of author contributions and competing interests; and statements of data and code availability are available at <https://doi.org/10.1038/s41589-024-01565-w>.

## References

1. Prior, I. A., Hood, F. E. & Hartley, J. L. The frequency of Ras mutations in cancer. *Cancer Res.* **80**, 2969–2974 (2020).
2. Ostrem, J. M., Peters, U., Sos, M. L., Wells, J. A. & Shokat, K. M. K-Ras(G12C) inhibitors allosterically control GTP affinity and effector interactions. *Nature* **503**, 548–551 (2013).
3. Hallin, J. et al. Anti-tumor efficacy of a potent and selective non-covalent KRASG12D inhibitor. *Nat. Med.* **28**, 2171–2182 (2022).
4. Kim, D. et al. Pan-KRAS inhibitor disables oncogenic signalling and tumour growth. *Nature* <https://doi.org/10.1038/s41586-023-06123-3> (2023).
5. Ma, N. et al. 2*H*-azirine-based reagents for chemoselective bioconjugation at carboxyl residues inside live cells. *J. Am. Chem. Soc.* **142**, 6051–6059 (2020).
6. McGrath, N. A., Andersen, K. A., Davis, A. K. F., Lomax, J. E. & Raines, R. T. Diazo compounds for the bioreversible esterification of proteins. *Chem. Sci.* **6**, 752–755 (2015).
7. Jun, J. V., Petri, Y. D., Erickson, L. W. & Raines, R. T. Modular diazo compound for the bioreversible late-stage modification of proteins. *J. Am. Chem. Soc.* **145**, 6615–6621 (2023).
8. Knox, J. E. et al. RM-036, a first-in-class, orally-bioavailable, Tri-Complex covalent KRASG12D(ON) inhibitor, drives profound anti-tumor activity in KRASG12D mutant tumor models. in *American Association for Cancer Research (AACR) Annual Meeting* (2022).
9. Zanon, P. R. A. et al. Profiling the proteome-wide selectivity of diverse electrophiles. Preprint at *ChemRxiv* <https://doi.org/10.26434/chemrxiv.14186561.v1> (2021).
10. Abbasov, M. E. et al. A proteome-wide atlas of lysine-reactive chemistry. *Nat. Chem.* **13**, 1081–1092 (2021).
11. Yang, T. et al. Reversible lysine-targeted probes reveal residence time-based kinase selectivity. *Nat. Chem. Biol.* **18**, 934–941 (2022).
12. Wan, X. et al. Discovery of lysine-targeted eIF4E inhibitors through covalent docking. *J. Am. Chem. Soc.* **142**, 4960–4964 (2020).
13. Chen, W. et al. Arylfluorosulfates inactivate intracellular lipid binding protein(s) through chemoselective SuFEx reaction with a binding site Tyr residue. *J. Am. Chem. Soc.* **138**, 7353–7364 (2016).
14. Zhang, Z., Guiley, K. Z. & Shokat, K. M. Chemical acylation of an acquired serine suppresses oncogenic signaling of K-Ras(G12S). *Nat. Chem. Biol.* **18**, 1177–1183 (2022).
15. Zheng, Q. et al. SuFEx-enabled, agnostic discovery of covalent inhibitors of human neutrophil elastase. *Proc. Natl Acad. Sci. USA* **116**, 18808–18814 (2019).
16. Zhang, Z., Morstein, J., Ecker, A. K., Guiley, K. Z. & Shokat, K. M. Chemoselective covalent modification of K-Ras(G12R) with a small molecule electrophile. *J. Am. Chem. Soc.* **144**, 15916–15921 (2022).
17. Gonzalez-Valero, A. et al. An activity-based oxaziridine platform for identifying and developing covalent ligands for functional allosteric methionine sites: redox-dependent inhibition of cyclin-dependent kinase 4. *J. Am. Chem. Soc.* **144**, 22890–22901 (2022).
18. Lowther, W. T., McMillen, D. A., Orville, A. M. & Matthews, B. W. The anti-angiogenic agent fumagillin covalently modifies a conserved active-site histidine in the *Escherichia coli* methionine aminopeptidase. *Proc. Natl Acad. Sci. USA* **95**, 12153–12157 (1998).
19. Jia, S., He, D. & Chang, C. J. Bioinspired thiophosphorodichloridate reagents for chemoselective histidine bioconjugation. *J. Am. Chem. Soc.* **141**, 7294–7301 (2019).
20. Cruite, J. T. et al. Cereblon covalent modulation through structure-based design of histidine targeting chemical probes. *RSC Chem. Biol.* **3**, 1105–1110 (2022).
21. McGregor, L. M., Jenkins, M. L., Kerwin, C., Burke, J. E. & Shokat, K. M. Expanding the scope of electrophiles capable of targeting K-Ras oncogenes. *Biochemistry* **56**, 3178–3183 (2017).
22. Wang, H.-L., Cee, V. J., Parsons, A. T. & Beaver, M. Pyridopyrimidine derivatives useful as KRAS G12C and KRAS G12D inhibitors in the treatment of cancer. WO 2021/081212 A1 (2021).
23. Yu, Z. et al. Simultaneous covalent modification of K-Ras(G12D) and K-Ras(G12C) with tunable oxirane electrophiles. *J. Am. Chem. Soc.* **145**, 20403–20411 (2023).
24. Robinson, S. L., Christenson, J. K. & Wackett, L. P. Biosynthesis and chemical diversity of β-lactone natural products. *Nat. Prod. Rep.* **36**, 458–475 (2019).
25. Hassan, A. Q. et al. The novolactone natural product disrupts the allosteric regulation of Hsp70. *Chem. Biol.* **22**, 87–97 (2015).
26. She, Y. M., Cheng, K. D., Farnsworth, A., Li, X. G. & Cyr, T. D. Surface modifications of influenza proteins upon virus inactivation by beta-propiolactone. *Proteomics* **13**, 3537–3547 (2013).
27. Logrippo, G. A. Investigations of the use of beta-propiolactone in virus inactivation. *Ann. N. Y. Acad. Sci.* **83**, 578–594 (1960).
28. Budowsky, E. I., Friedman, E. A., Zheleznova, N. V. & Noskov, F. S. Principles of selective inactivation of viral genome. VI. Inactivation of the infectivity of the influenza virus by the action of beta-propiolactone. *Vaccine* **9**, 398–402 (1991).
29. Fan, C. et al. Beta-propiolactone inactivation of coxsackievirus A16 induces structural alteration and surface modification of viral capsids. *J. Virol.* **91**, 10-1128 (2017).
30. Gao, Q. et al. Development of an inactivated vaccine candidate for SARS-CoV-2. *Science* **369**, 77–81 (2020).
31. Wang, H. et al. Development of an inactivated vaccine candidate, BBIBP-CorV, with potent protection against SARS-CoV-2. *Cell* **182**, 713–721 (2020).
32. Böttcher, T. & Sieber, S. A. β-Lactams and β-lactones as activity-based probes in chemical biology. *MedChemComm* **3**, 408–417 (2012).
33. Zhang, Y., Gross, R. A. & Lenz, R. W. Stereochemistry of the ring-opening polymerization of (S)-β-butyrolactone. *Macromolecules* **23**, 3206–3212 (1990).



34. Hansen, R. et al. The reactivity-driven biochemical mechanism of covalent KRAS(G12C) inhibitors. *Nat. Struct. Mol. Biol.* **25**, 454–462 (2018).
35. Wang, X. et al. KRAS G12D inhibitors. WO/2021/041671 (2021).
36. Vasta, J. D. et al. KRAS is vulnerable to reversible Switch-II Pocket engagement in cells. *Nat. Chem. Biol.* **18**, 596–604 (2022).
37. Wang, X. et al. Identification of MRTX1133, a noncovalent, potent, and selective KRAS(G12D) inhibitor. *J. Med. Chem.* **65**, 3123–3133 (2022).
38. Keats, M. A., Han, J. J. W., Lee, Y.-H., Lee, C.-S. & Luo, J. A non-conserved histidine residue on KRAS drives paralog selectivity of the KRASG12D inhibitor MRTX1133. *Cancer Res.* **83**, 2816–2823 (2023).
39. Janes, M. R. et al. Targeting KRAS mutant cancers with a covalent G12C-specific inhibitor. *Cell* **172**, 578–589 (2018).
40. Lanman, B. A. et al. Discovery of a covalent inhibitor of KRAS(G12C) (AMG 510) for the treatment of solid tumors. *J. Med. Chem.* **63**, 52–65 (2020).
41. Fell, J. B. et al. Identification of the clinical development candidate MRTX849, a covalent KRAS(G12C) inhibitor for the treatment of cancer. *J. Med. Chem.* **63**, 6679–6693 (2020).
42. Lorthiois, E. et al. JDQ443, a structurally novel, pyrazole-based, covalent inhibitor of KRASG12C for the treatment of solid tumors. *J. Med. Chem.* **65**, 16173–16203 (2022).
43. Schulze, C. J. et al. Chemical remodeling of a cellular chaperone to target the active state of mutant KRAS. *Science* **381**, 794–799 (2023).
44. Zhang, Z. et al. GTP-state-selective cyclic peptide ligands of K-Ras(G12D) block its interaction with Raf. *ACS Cent. Sci.* **6**, 1753–1761 (2020).
45. Hunter, J. C. et al. Biochemical and structural analysis of common cancer-associated KRAS mutations. *Mol. Cancer Res* **13**, 1325–1335 (2015).
46. Olson, A. R. & Miller, R. J. The mechanism of the aqueous hydrolysis of  $\beta$ -butyrolactone. *J. Am. Chem. Soc.* **60**, 2687–2692 (1938).
47. Fujioka, A. et al. Dynamics of the Ras/ERK MAPK cascade as monitored by fluorescent probes. *J. Biol. Chem.* **281**, 8917–8926 (2006).
48. Peacock, D. M., Kelly, M. J. S. & Shokat, K. M. Probing the KRas Switch II groove by fluorine NMR spectroscopy. *ACS Chem. Biol.* **17**, 2710–2715 (2022).
49. Asai, A., Hasegawa, A., Ochiai, K., Yamashita, Y. & Mizukami, T. Belactosin A, a novel antitumor antibiotic acting on cyclin/CDK mediated cell cycle regulation, produced by *Streptomyces* sp. *J. Antibiot.* **53**, 81–83 (2000).
50. Kawamura, S. et al. Potent proteasome inhibitors derived from the unnatural cis-cyclopropane isomer of belactosin A: synthesis, biological activity, and mode of action. *J. Med. Chem.* **56**, 3689–3700 (2013).
51. Kawamura, S., Unno, Y., Asai, A., Arisawa, M. & Shuto, S. Design and synthesis of the stabilized analogs of belactosin A with the unnatural cis-cyclopropane structure. *Org. Biomol. Chem.* **11**, 6615–6622 (2013).
52. Warmuth, M., Kim, S., Gu, X.-J., Xia, G. & Adrián, F. Ba/F3 cells and their use in kinase drug discovery. *Curr. Opin. Oncol.* **19**, 55–60 (2007).
53. Mayr, H. & Patz, M. Scales of nucleophilicity and electrophilicity: a system for ordering polar organic and organometallic reactions. *Angew. Chem. Int. Ed. Engl.* **33**, 938–957 (1994).
54. Lito, P., Solomon, M., Li, L.-S., Hansen, R. & Rosen, N. Allele-specific inhibitors inactivate mutant KRAS G12C by a trapping mechanism. *Science* **351**, 604–608 (2016).
55. Mix, K. A., Lomax, J. E. & Raines, R. T. Cytosolic delivery of proteins by bioreversible esterification. *J. Am. Chem. Soc.* **139**, 14396–14398 (2017).

**Publisher's note** Springer Nature remains neutral with regard to jurisdictional claims in published maps and institutional affiliations.

**Open Access** This article is licensed under a Creative Commons Attribution 4.0 International License, which permits use, sharing, adaptation, distribution and reproduction in any medium or format, as long as you give appropriate credit to the original author(s) and the source, provide a link to the Creative Commons licence, and indicate if changes were made. The images or other third party material in this article are included in the article's Creative Commons licence, unless indicated otherwise in a credit line to the material. If material is not included in the article's Creative Commons licence and your intended use is not permitted by statutory regulation or exceeds the permitted use, you will need to obtain permission directly from the copyright holder. To view a copy of this licence, visit <http://creativecommons.org/licenses/by/4.0/>.

© The Author(s) 2024

## Methods

### Ethics of animal use

All animal studies were performed at Crown Bioscience (San Diego, CA). All the animal study procedures were performed in the specific-pathogen-free animal facility at Crown Bioscience under the approved protocols by the Institutional Animal Care and Use Committee, with the guidance of the Association for Assessment and Accreditation of Laboratory Animal Care.

### Chemical synthesis and characterizations

Synthetic procedures and characterizations of new compounds are reported in Supplementary Information.

### Recombinant protein expression and purification

K-Ras-WT, K-Ras-G12D, K-Ras-G12E, K-Ras-G13D and K-Ras-G12D Cyslight DNA sequences encoding human K-Ras (WT, a.a. 1–169), human K-Ras (G12D, a.a. 1–169), human K-Ras (G12E, a.a. 1–169), human K-Ras (G13D, a.a. 1–169) and human K-Ras G12D Cyslight (G12D/C51S/C80L/C118S, a.a. 1–169) were codon optimized, synthesized by Twist Biosciences and cloned into pJExpress411 vector using the Gibson Assembly method<sup>7</sup>. The resulting construct contains N-terminal 6xHis tag and a Tobacco Etch Virus (TEV) protease cleavage site (ENLYFQG). The proteins were expressed and purified following previously reported protocols<sup>2,8</sup>. Briefly, chemically competent BL21(DE3) cells were transformed with the corresponding plasmid and grown on LB agar plates containing 50  $\mu\text{g ml}^{-1}$  kanamycin. A single colony was used to inoculate a culture at 37 °C, 220 rpm in terrific broth containing 50  $\mu\text{g ml}^{-1}$  kanamycin. When the optical density reached 0.6, the culture temperature was reduced to 20 °C, and protein expression was induced by the addition of isopropyl  $\beta$ -D-1-thiogalactopyranoside to 1 mM. After 16 h at 20 °C, the cells were pelleted by centrifugation (6,500g, 10 min) and lysed in lysis buffer (20 mM Tris 8.0, 500 mM NaCl and 5 mM imidazole) with a high-pressure homogenizer (Microfluidics). The lysate was clarified by high-speed centrifugation (19,000g, 15 min) and the supernatant was used in subsequent purification by immobilized metal affinity chromatography. His-TEV-tagged protein was captured with Co-TALON resin (Clontech, Takara Bio, 2 ml slurry per liter culture) at 4 °C for 1 h with constant end-to-end mixing. The loaded beads were then washed with lysis buffer (50 ml per liter culture), and the protein was eluted with elution buffer (20 mM Tris 8.0, 300 mM NaCl and 300 mM imidazole). To this protein solution was added His-tagged TEV protease (0.05 mg TEV per milligram Ras protein) and GDP (1 mg per milligram Ras protein), and the mixture was dialyzed against TEV cleavage buffer (20 mM Tris 8.0, 300 mM NaCl, 1 mM ethylenediaminetetraacetic acid and 1 mM DTT) at 4 °C using a 10 K molecular weight cutoff (MWCO) dialysis cassette until liquid chromatography (LC)–MS analysis showed full cleavage (typically 16–24 h).  $\text{MgCl}_2$  was added to a final concentration of 5 mM, and the mixture was incubated with 1 ml Ni-NTA (Qiagen) beads at 4 °C for 1 h to remove TEV protease, any residual His-tagged proteins and peptides. The protein solution was diluted 1:10 v/v with 20 mM Tris 8.0 and further purified with anion exchange chromatography (HiTrapQ column, GE Healthcare Life Sciences) using a NaCl gradient of 50 mM to 500 mM in 20 mM Tris 8.0. Nucleotide loading was performed by mixing the ion exchange-purified protein with an excess of GDP (5 mg per liter culture) or GppNHp (5 mg per liter culture) and 5 mM ethylenediaminetetraacetic acid at 23 °C for 30 min. The reaction was stopped by the addition of  $\text{MgCl}_2$  to 10 mM. For GppNHp, an additional calf intestine phosphatase treatment was performed as follows to ensure high homogeneity of the loaded nucleotide. The protein buffer was exchanged into phosphatase buffer (32 mM Tris 8.0, 200 mM ammonium sulfate and 0.1 mM  $\text{ZnCl}_2$ ) with a HiTrap Desalting Column (GE Healthcare Life Sciences). To the buffer-exchanged protein solutions, GppNHp was added to 5  $\text{mg ml}^{-1}$ , and calf intestine phosphatase (NEB) was added to 10 U  $\text{ml}^{-1}$ . The reaction mixture was incubated on ice for 1 h, and  $\text{MgCl}_2$  was added to a final concentration

of 20 mM. After nucleotide loading, the protein was concentrated using an 10 K MWCO centrifugal concentrator (Amicon-15, Millipore) to 20  $\text{mg ml}^{-1}$  and purified by size exclusion chromatography on a Superdex 75 10/300 GL column (GE Healthcare Life Sciences). Fractions containing pure Ras protein were pooled and concentrated to 20  $\text{mg ml}^{-1}$  and stored at  $-80$  °C. In our hands, this protocol gives a typical yield of 5–15 mg per liter culture.

### Crystallization

K-Ras-G12D Cyslight (G12D/C51S/C80L/C118S) bound by GDP purified by size exclusion chromatography was diluted to 20  $\mu\text{M}$  in reaction buffer (20 mM HEPES 7.5, 150 mM NaCl and 1 mM  $\text{MgCl}_2$ ). Compound 1 was added as a 10 mM solution in dimethyl sulfoxide (DMSO) to a final concentration of 50  $\mu\text{M}$ . The mixture was allowed to stand at 23 °C until LC–MS analysis of the reaction mixture showed full conversion to a single covalent adduct. The reaction mixture was concentrated using a 10 K MWCO filter device and the adduct was purified by size exclusion chromatography (Superdex 75, 20 mM HEPES 7.5, 150 mM NaCl and 1 mM  $\text{MgCl}_2$ ) and concentrated to 20  $\text{mg ml}^{-1}$ . For crystallization, 0.1  $\mu\text{l}$  of the protein was mixed with 0.1  $\mu\text{l}$  well buffer containing 0.1 M MES 6.5, 25% PEG4K. Crystals were grown at 20 °C in a 96-well plate using the hanging-drop vapor diffusion method. Maximal crystal growth was achieved after 7 days. The crystals were transferred to a cryoprotectant solution (0.1 M MES 6.5, 25% PEG4K and 25% glycerol) and flash-frozen in liquid nitrogen.

### X-ray data collection and structure determination

The dataset was collected at the Advanced Light Source beamline 8.2.2 with X-ray at a wavelength of 0.999907 Å. The dataset was indexed and integrated using iMosflm<sup>56</sup>, scaled with Scala<sup>57</sup> and solved by molecular replacement using Phaser<sup>58</sup> in CCP4 software suite<sup>59</sup>. The crystal structure of GDP-bound K-Ras-G12C-MRTX849 adduct (PDB code 6USZ) was used as the initial model. The structure was manually refined with Coot<sup>60</sup> and PHENIX<sup>61</sup>. Data collection and refinement statistics are listed in Supplementary Table 1. In the Ramachandran plot of the final structure, 98.21% and 1.49% of the residues are in the favored regions and allowed regions, respectively.

### Cell culture

AsPc-1 (CRL-1682), SW1990 (CRL-2172), H1299 (or NCI-H1299, CRL-5803), HCT-116 (CCL-247), A549 (CRM-CCL-185), A375 (or A-375, CRL-1619), HEK293 (CRL-1573) cells were obtained from ATCC and maintained in high-glucose (4.5 g  $\text{l}^{-1}$ ) DMEM (Gibco 11995073) supplemented with 4 mM L-glutamine, 1 mM sodium pyruvate and 10% heat-inactivated fetal bovine serum (FBS; Axenia Biologix). AGS (CRL-1739) cells were obtained from ATCC and maintained in Ham's F12-K (Gibco 21127022) supplemented with 10% heat-inactivated FBS (Axenia Biologix). Ba/F3 cells were a gift from Dr. Trever Bivona (University of California, San Francisco) and were maintained in RPMI-1640 (Gibco 11875093) supplemented with 10% heat-inactivated FBS (Axenia Biologix) and 10  $\text{ng ml}^{-1}$  recombinant mouse IL-3 (Gibco PMC0031).

Cells were passed for at least two generations after cryorecovery before they were used for assays. All cell lines were tested mycoplasma negative using MycoAlert Mycoplasma Detection Kit (Lonza).

### Gel electrophoresis and immunoblotting

Cells were treated with drugs at 40–60% confluency at a final DMSO concentration of 1%. At the end of the treatment period, cells were chilled on ice. Unless otherwise indicated, adherent cells were washed once with ice-cold PBS (1 ml), scraped with a spatula, and pelleted by centrifugation (500g, 5 min). Suspension cells were pelleted by centrifugation (500g, 5 min), washed with 1 ml ice-cold PBS, and pelleted again. Cells were lysed in RIPA buffer supplemented with protease and phosphatase inhibitors (mini cOmplete and phosSTOP, Roche) on ice for 10 min. Concentrations of lysates were determined with protein

BCA assay (Thermo Fisher) and adjusted to 2 mg ml<sup>-1</sup> or lowest available concentration with additional RIPA buffer. Samples were mixed with 5× sodium dodecyl sulfate (SDS) loading dye and denatured at either room temperature for 30 min for Ras band shift experiment, or 95 °C for 5 min for other non-Ras proteins immunoblotting. Note: protein denaturation with 5× SDS loading dye at elevated temperature caused hydrolysis of covalent K-Ras-G12D-malolactone adducts due to the action of DTT. The same covalent complex remained stable at room temperature with 500 mM DTT.

Unless otherwise noted, SDS–polyacrylamide gel electrophoresis was run with Novex 12% Bis-Tris gel (Invitrogen) in MOPS running buffer (Invitrogen) at 200 V for 60 min following the manufacturer's instructions. Proteins were transferred onto 0.2-µm nitrocellulose membranes (Bio-Rad) using a wet-tank transfer apparatus (Bio-Rad Criterion Blotter) in 1× TOWBIN buffer with 10% methanol at 75 V for 45 min. Membranes were blocked in 5% bovine serum albumin (BSA)–tris-buffered saline-Tween 20 (TBST) for 1 h at 23 °C. Primary antibody binding was performed with the indicated antibodies diluted in 5% BSA–TBST at 4 °C for at least 16 h. After washing the membrane three times with TBST (5 min each wash), secondary antibodies (goat anti-rabbit IgG-IRDye 800 and goat anti-mouse IgG-IRDye 680, Li-COR) were added as solutions in 5% BSA–TBST at the dilutions recommended by the manufacturer. Secondary antibody binding was allowed to proceed for 1 h at 23 °C. The membrane was washed three times with TBST (5 min each wash) and imaged on a Li-COR Odyssey fluorescence imager.

### Preparation of MSCV

pMSCV-Puro plasmids (where MSCV is mouse stem cell virus) containing full-length human *KRAS* genes (WT, G12D) were constructed using standard molecule biology techniques by inserting the *KRAS* gene fragment between the BamHI and XhoI sites. Transfection-grade plasmids were prepared using ZymoPure II Plasmid Midiprep kit. EcoPack 293 cells (Takara Bio) were plated in six-well plates (3 × 10<sup>5</sup> ml<sup>-1</sup>, 2 ml). The next day, cells were transfected with 2.5 µg pMSCV plasmid using Lipofectamine 3000 following the manufacturer's instructions. The cells were incubated for 66 h, and then the virus-containing supernatants were collected and passed through a 0.22-µm syringe filter. The collected virus was used immediately for spinfection of Ba/F3 cells or stored at –80 °C.

### Generation of stable Ba/F3 transductants

One milliliter of MSCV-containing supernatant (vide supra) was added to one well of a six-well plate containing 1 × 10<sup>6</sup> Ba/F3 cells in 1 ml of medium composed of 60% RPMI 1640, 40% heat-inactivated fetal bovine serum (FBS), 10 ng mouse IL-3 and 4 µg polybrene. Cells were spininfected by centrifugation at 2,000g for 90 min at room temperature and then placed in the incubator for 24 h. After 1 day, the cells were diluted into 10 ml culture medium (RPMI 1640 + 10% heat-inactivated FBS, 10 ng ml<sup>-1</sup> mouse IL-3) and recovered for a second day after spinfection. On the third day after spinfection, cells were pelleted at 500g for 5 min and resuspended in 10 ml selection medium (RPMI 1640 + 10% heat-inactivated FBS, 10 ng ml<sup>-1</sup> mouse IL-3 and 1.25 µg ml<sup>-1</sup> puromycin). Cells were maintained under puromycin selection for 4–7 days, splitting as required to maintain density <2 × 10<sup>6</sup> cells ml<sup>-1</sup>. After 7 days, cells were pelleted, washed once with IL-3 free culture medium (RPMI 1640 + 10% heat-inactivated FBS) and pelleted again before resuspending at 2–4 × 10<sup>5</sup> cells ml<sup>-1</sup> in IL-3 free culture medium. Cells were maintained under these conditions for 7 days, passaging as needed to maintain density <2 × 10<sup>6</sup> cells ml<sup>-1</sup>. Growth was monitored (Countess II Cell Counter) over these 7 days to confirm that an IL-3 independent population has been achieved.

### Differential scanning fluorimetry

The protein of interest was diluted with SEC buffer (20 mM HEPES 7.5, 150 mM NaCl and 1 mM MgCl<sub>2</sub>) to 2 µM. This solution was dispensed into

wells of a white 96-well polymerase chain reaction plate in triplicate (25 µl per well). Fluorescence was measured at 0.5 °C temperature intervals every 30 s from 25 °C to 95 °C on a Bio-Rad CFX96 qPCR system using the FRET setting. Each dataset was normalized to the highest fluorescence and the normalized fluorescence reading was plotted against temperature in GraphPad Prism 9.0. *T<sub>m</sub>* values were determined as the temperature(s) corresponding to the maximum (or maxima) of the first derivative of the curve. Proteins crosslinked with small molecules were desalted using Zeba Spin Desalting Columns (Thermo) before differential scanning fluorimetry *T<sub>m</sub>* measurement.

### Detection of covalent modification of K-Ras by whole-protein MS

Test compounds were prepared as 100× stock solutions in DMSO. K-Ras proteins were diluted with SEC buffer (20 mM HEPES 7.5, 150 mM NaCl and 1 mM MgCl<sub>2</sub>) to 1 µM. In a typical reaction, 1 µl 100× compound stock was mixed with 99 µl diluted K-Ras protein, and the resulting mixture was incubated for the desired amount of time. The extent of modification was assessed by electrospray MS using a Waters Xevo G2-XS system equipped with an Acquity UPLC BEH C4 1.7 µm column. The mobile phase was a linear gradient of 5–95% acetonitrile/water + 0.05% formic acid. For kinetic measurements, a 2× compound solution was first prepared in SEC buffer, which was then mixed with 400 nM K-Ras-G12D protein at 1:1 (v/v) ratio. Injection time stamps were used to calculate elapsed time.

### Detection of covalent modification of K-Ras by tandem MS

K-Ras-G12D protein (1 µM, 100 µl) in PBS 7.4 was treated with β-propiolactone (1 mM or 10 mM) at 23 °C for 1 h. The reaction buffer was exchanged into digestion buffer (20 mM Tris 8.0 and 2 mM CaCl<sub>2</sub>) using a Zeba 0.5-ml desalting column (7 KMWCO, Thermo Scientific). Eighty microliters of the resulting protein solution was mixed with 2 µl 200 mM DTT. The mixture was heated at 56 °C for 30 min. After cooling to 23 °C, 4 µl 200 mM iodoacetamide was added. After 15 min at 23 °C, 2.1 µl 200 mM DTT was added. After an additional 5 min, 500 ng trypsin was added to the mixture, and the samples were incubated at 37 °C overnight. Five microliters 10% formic acid was added to stop the digestion (final formic acid concentration 0.5% v/v). The tryptic peptides were enriched and desalted using OMIX C18 tips (Agilent) following the manufacturer's instructions. Peptides (0.5% of total) were resolved on an Easy-Spray nano-HPLC column (Thermo Fisher ES800A, 150 mm length, 3 µl particle size, 100-Å particle size) over a 54-min gradient of 2–37% acetonitrile–water + 0.1% formic acid and analyzed by a Q-Exactive hybrid quadrupole-Orbitrap mass spectrometer (MS1 resolution: 70,000; automatic gain control (AGC) target, 3 × 10<sup>6</sup>; range, 350–1,500 *m/z*; MS2 resolution: 17,500; AGC target, 5 × 10<sup>4</sup>; maximum injection time, 120 ms; Top 10: NCE, 25%; dynamic exclusion, 15 s). Peptides were searched against the K-Ras-G12D sequence using MaxQuant (v.2.0.3.0, <https://www.maxquant.org/>), with β-propiolactone (C<sub>3</sub>H<sub>4</sub>O<sub>2</sub>) as a variable modification on serine, threonine, lysine, aspartate, tyrosine, glutamate and histidine residues. Peptides were identified with a false discovery rate cutoff of 0.01. Only the peptides with sufficient MS2 fragment information to assign the modification site with >0.9 probability were used for analysis.

### Stability of β-lactone compounds in PBS

Ten-micromolar solution of β-lactone compound in PBS, pH 7.4 was prepared by diluting 1 µl of 10 mM DMSO stock solution into 999 µl of PBS pH 7.4 in the presence or absence of 5 mM reduced GSH. At specified time points, aliquots were taken, and the amount of intact compound was analyzed on a Waters Xevo G2-XS Quadrupole-TOF system equipped with an Acquity UPLC BEH C18 1.7 µm column for multiple-reaction monitoring for the 1+ precursor of respective compound (precursor > precursor) with target enhancement and low collision energy (0–2 eV).

### 2D cell viability assay

Cells were seeded into 96-well white flat-bottom plates (1,000 cells per well) (Greiner Bio-One, 655083) and incubated overnight. Cells were treated with the indicated compounds in a nine-point threefold dilution series (100  $\mu$ l final volume) and incubated for 72 h. Cell viability was assessed using a commercial CellTiter-Glo (CTG) luminescence-based assay (Promega). The 96-well plates were equilibrated to room temperature before the addition of diluted CTG reagent (100  $\mu$ l) (1:4 CTG reagent:PBS, containing 1% Triton X-100). Plates were placed on an orbital shaker for 30 min before recording luminescence using a Spark 20M (Tecan) plate reader.

### 3D cell viability assay

Cells were resuspended in fresh culture medium to a concentration of (1,000 cells per well) and plated (90  $\mu$ l per well) in Corning Costar 3474, 96-well clear flat-bottom ultralow-attachment microplates. Cells were treated with the indicated compounds in a nine-point threefold dilution series (100  $\mu$ l final volume) and incubated for 120 h. Cell viability was assessed using a commercial CTG luminescence-based assay (Promega) as described in 2D cell viability assay.

### Animal studies

All animal studies were performed at Crown Bioscience (San Diego, CA). Six- to 9-week-old female mice (NOD/SCID) were purchased from the Jackson Laboratory. SW1990 xenografts were established by subcutaneous injection into the rear flanks of mice with SW1990 cells ( $5 \times 10^6$  cells in 100  $\mu$ l of serum-free medium mixed 1:1 with Matrigel). Tumor xenografts were allowed to establish, and mice were randomized into control and treatment groups when tumors reached a size range of 200–400 mm<sup>3</sup>. Dosing of (R)-G12Di-7 (10 or 50 mg kg<sup>-1</sup> in 5% DMSO, 10% captisol in 1 $\times$  PBS pH 7.4) or vehicle control (5% DMSO, 10% captisol in 1 $\times$  PBS pH 7.4) was administered twice a day via intraperitoneal route. Tumor volume was assessed biweekly and body weight was assessed daily for the duration of the study. Tumor volume was assessed by caliper 2D measurement, and volume was calculated using the following formula to approximate the volume: (longest diameter  $\times$  shortest diameter<sup>2</sup>)/2.

### Reporting summary

Further information on research design is available in the Nature Portfolio Reporting Summary linked to this article.

### Data availability

Atomic coordinates and structure factors for the reported crystal structure have been deposited with the PDB, with the following accession numbers: K-Ras-G12D•GDP•(RS)-G12Di-1, [8T4V](https://doi.org/10.1038/s41589-024-01565-w). Additional data used in this study are PDB [7PRZ](https://doi.org/10.1038/s41589-024-01565-w), [6UTO](https://doi.org/10.1038/s41589-024-01565-w) and [6OIM](https://doi.org/10.1038/s41589-024-01565-w). Protein sequences used in this study could be accessed at Uniprot (<https://uniprot.org>) with the following accession code: [P01116](https://uniprot.org) (K-Ras, the 1–169 truncated form was used). Source data are provided with this paper.

### References

- Battye, T. G., Kontogiannis, L., Johnson, O., Powell, H. R. & Leslie, A. G. iMOSFLM: a new graphical interface for diffraction-image processing with MOSFLM. *Acta Crystallogr. D* **67**, 271–281 (2011).
- Evans, P. Scaling and assessment of data quality. *Acta Crystallogr. D* **62**, 72–82 (2006).
- McCoy, A. J. et al. Phaser crystallographic software. *J. Appl. Crystallogr.* **40**, 658–674 (2007).

- Winn, M. D. et al. Overview of the CCP4 suite and current developments. *Acta Crystallogr. D* **67**, 235–242 (2011).
- Emsley, P., Lohkamp, B., Scott, W. G. & Cowtan, K. Features and development of Coot. *Acta Crystallogr. D* **66**, 486–501 (2010).
- Adams, P. D. et al. PHENIX: a comprehensive Python-based system for macromolecular structure solution. *Acta Crystallogr. D* **66**, 213–221 (2010).

### Acknowledgements

Q.Z. is the Connie and Bob Lurie Fellow of the Damon Runyon Cancer Research Foundation (DRG-2434-21). Z.Z. was supported by a Damon Runyon Fellow supported by the Damon Runyon Cancer Research Foundation (DRG-2281-17). K.Z.G. was supported as an HHMI Fellow by the Damon Runyon Cancer Research Foundation (DRG-2399-20). K.M.S. acknowledges support from the NIH (5R01CA244550), HHMI and The Waxman Foundation for Cancer Research. Q.Z. acknowledges support from the UCSF Pancreas Center via a Mentored Scientist Award. We thank J. Taunton and Z. Knight for helpful advice.

### Author contributions

Q.Z., Z.Z. and K.M.S. conceptualized this study, wrote the original draft, and reviewed and edited the manuscript. Q.Z. and Z.Z. synthesized, characterized and tested compounds in biochemical and cell-based assays, and analyzed data. Q.Z. designed and analyzed animal studies. Z.Z. and K.Z.G. collected and analyzed crystallization data.

### Competing interests

K.M.S., Z.Z. and Q.Z. are inventors on patents related to covalent K-Ras-G12D inhibitors reported here. K.M.S. is an inventor on patents owned by University of California San Francisco covering KRAS targeting small molecules licensed to Araxes, Erasca and Novartis. K.M.S. has consulting agreements for the following companies, which involve monetary and/or stock compensation: BioTheryX, BridGene Biosciences, eFFECTOR Therapeutics, Erasca, G Protein Therapeutics, Ikena, Initial Therapeutics, Kumquat Biosciences, Kura Oncology, Merck, Mitokinin, Nested, Nextech, Novartis, Radd Pharma, Revolution Medicines, Rezo, Totus, Turning Point, Type6 Therapeutics, Vevo, Vicinitas and Wellspring Biosciences (Araxes Pharma). The remaining authors declare no competing interests.

### Additional information

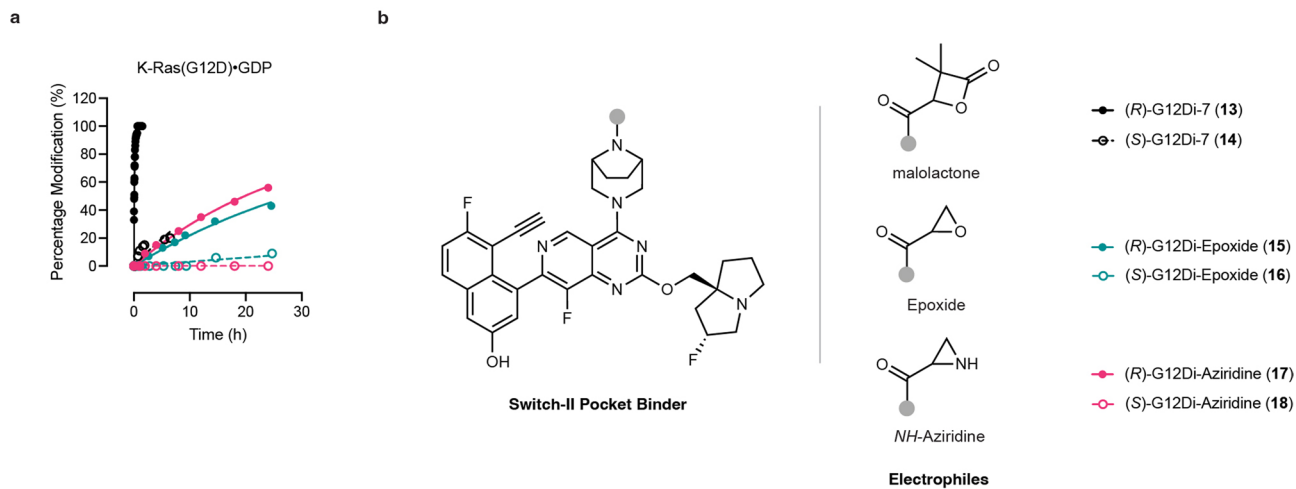
**Extended data** is available for this paper at <https://doi.org/10.1038/s41589-024-01565-w>.

**Supplementary information** The online version contains supplementary material available at <https://doi.org/10.1038/s41589-024-01565-w>.

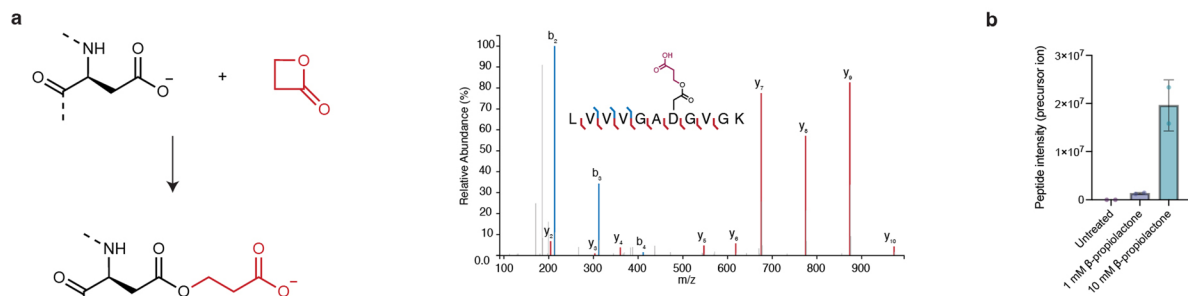
**Correspondence and requests for materials** should be addressed to Ziyang Zhang or Kevan M. Shokat.

**Peer review information** *Nature Chemical Biology* thanks Benjamin Cravatt, Akio Ojida and the other, anonymous, reviewers for their contribution to the peer review of this work.

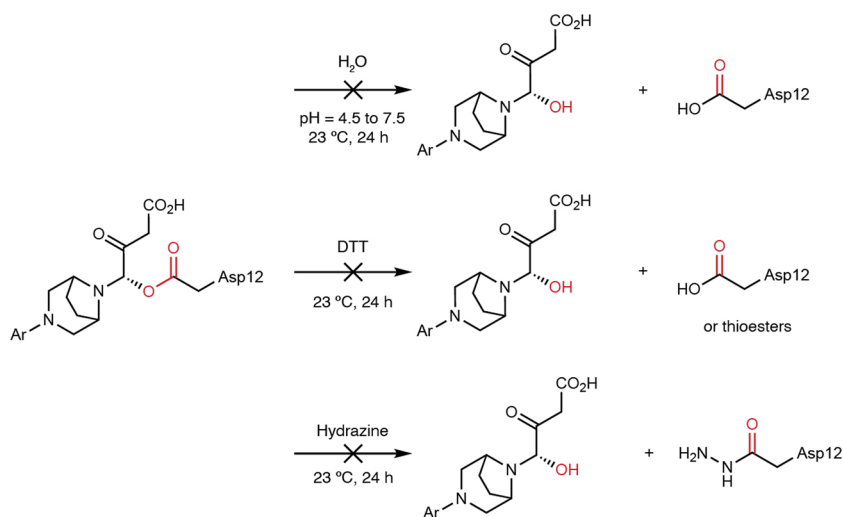
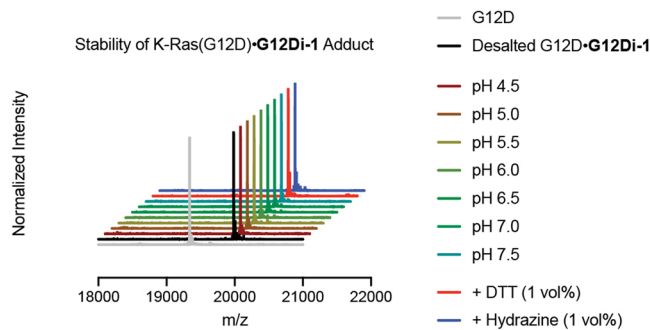
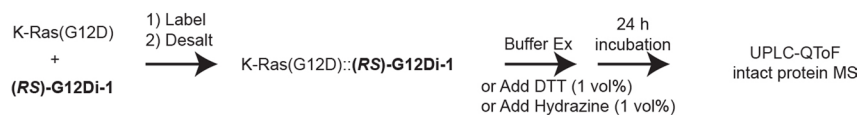
**Reprints and permissions information** is available at [www.nature.com/reprints](http://www.nature.com/reprints).



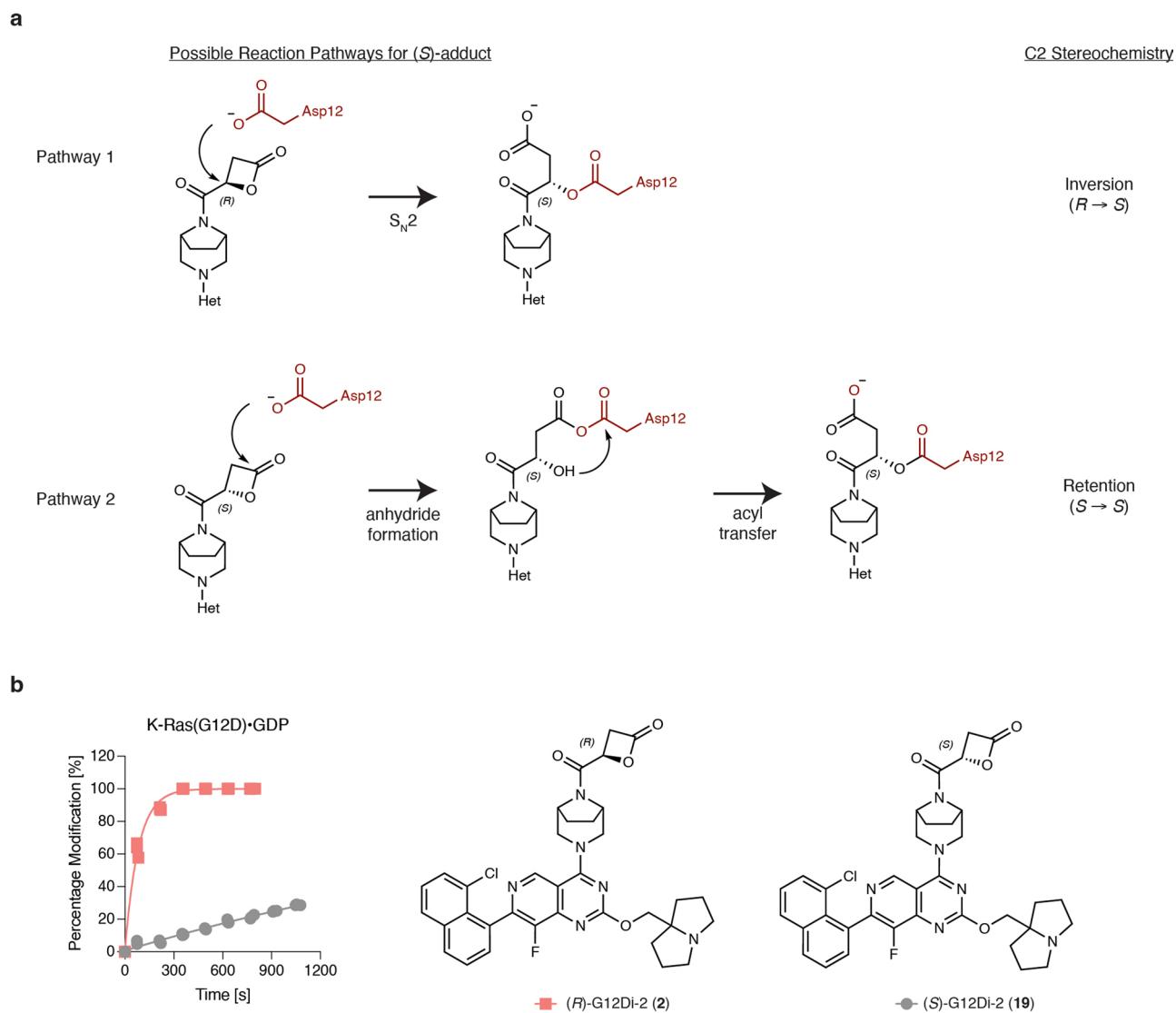
**Extended Data Fig. 1 | Covalent modification of K-Ras-G12D by strain-release electrophiles. a**, Covalent labeling kinetics. Conditions: 200 nM K-Ras-G12D•GDP, 10  $\mu$ M compound, 20 mM HEPES pH 7.5, 150 mM MgCl<sub>2</sub>, 23 °C. **b**, Chemical structures of strain-release electrophiles.



**Extended Data Fig. 2 |  $\beta$ -Propiolactone covalently labeled Asp12 of recombinant K-Ras-G12D. a,** Alkylation of Asp12 by  $\beta$ -propiolactone and identified fragment ions of aa. 6-16 peptide including covalently modified Asp12. **b,** Extent of covalent modification is dose dependent. All data points represent individual biological replicates. Data are presented as mean  $\pm$  SD ( $n = 2$ ).

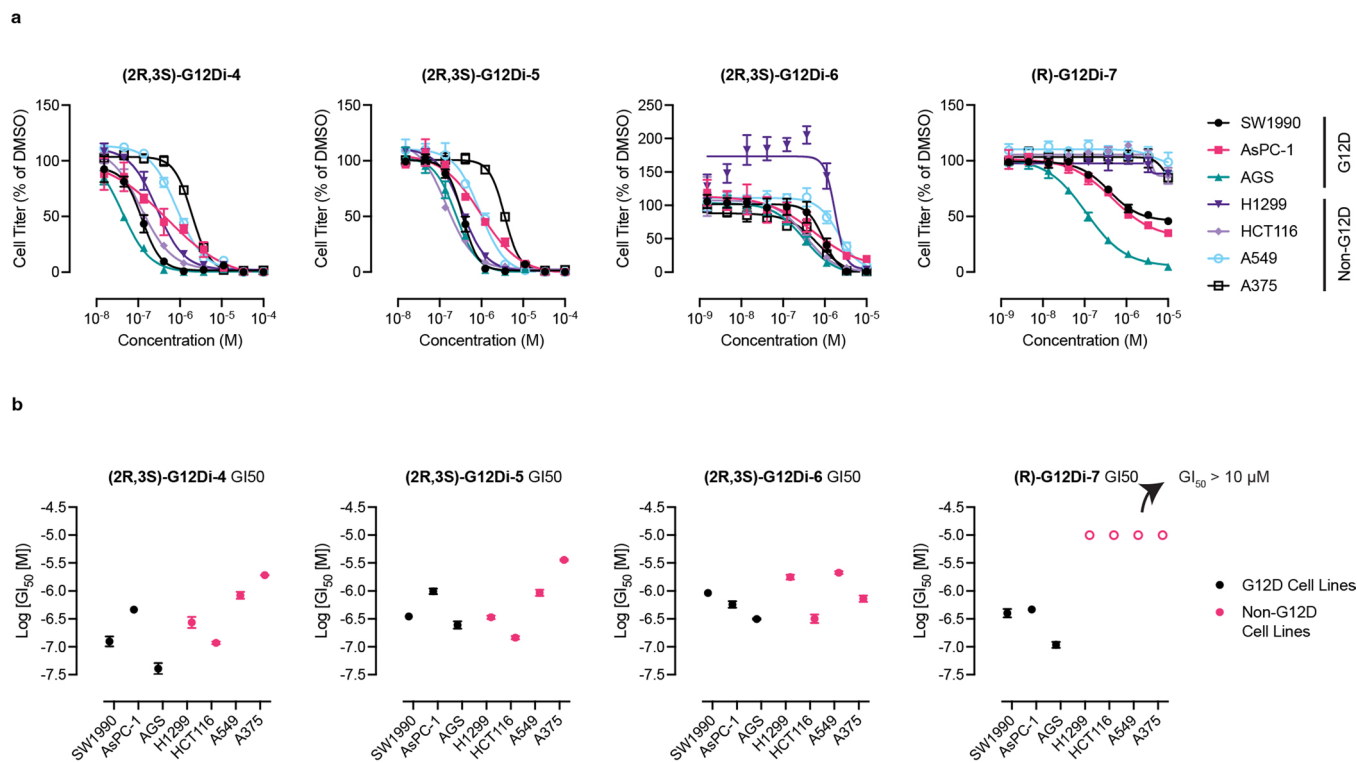


**Extended Data Fig. 3 | Covalent K-Ras-G12D-1 adduct is stable in pH 4.5–7.5 buffers and to thiol (DTT) or amine (hydrazine) electrophiles. Mass spectra are representative of two independent experiments.**

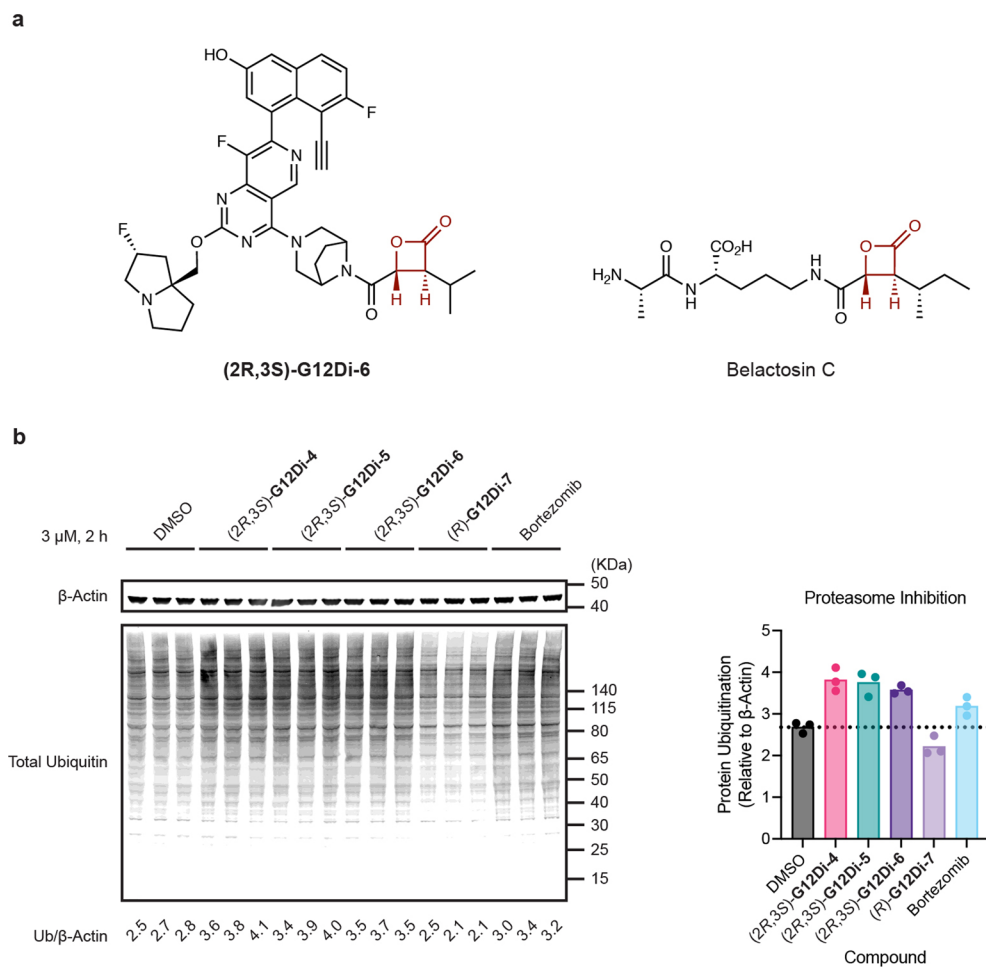


**Extended Data Fig. 4 | Mechanistic rationale of the enantioselectivity of the covalent modification reaction. a**, Two possible reaction pathways to form (*S*)-adduct with distinct stereochemical events at  $\alpha$ -carbon. **b**, K-Ras-G12D favors an (*R*)-enantiomer of the malolactone electrophile.

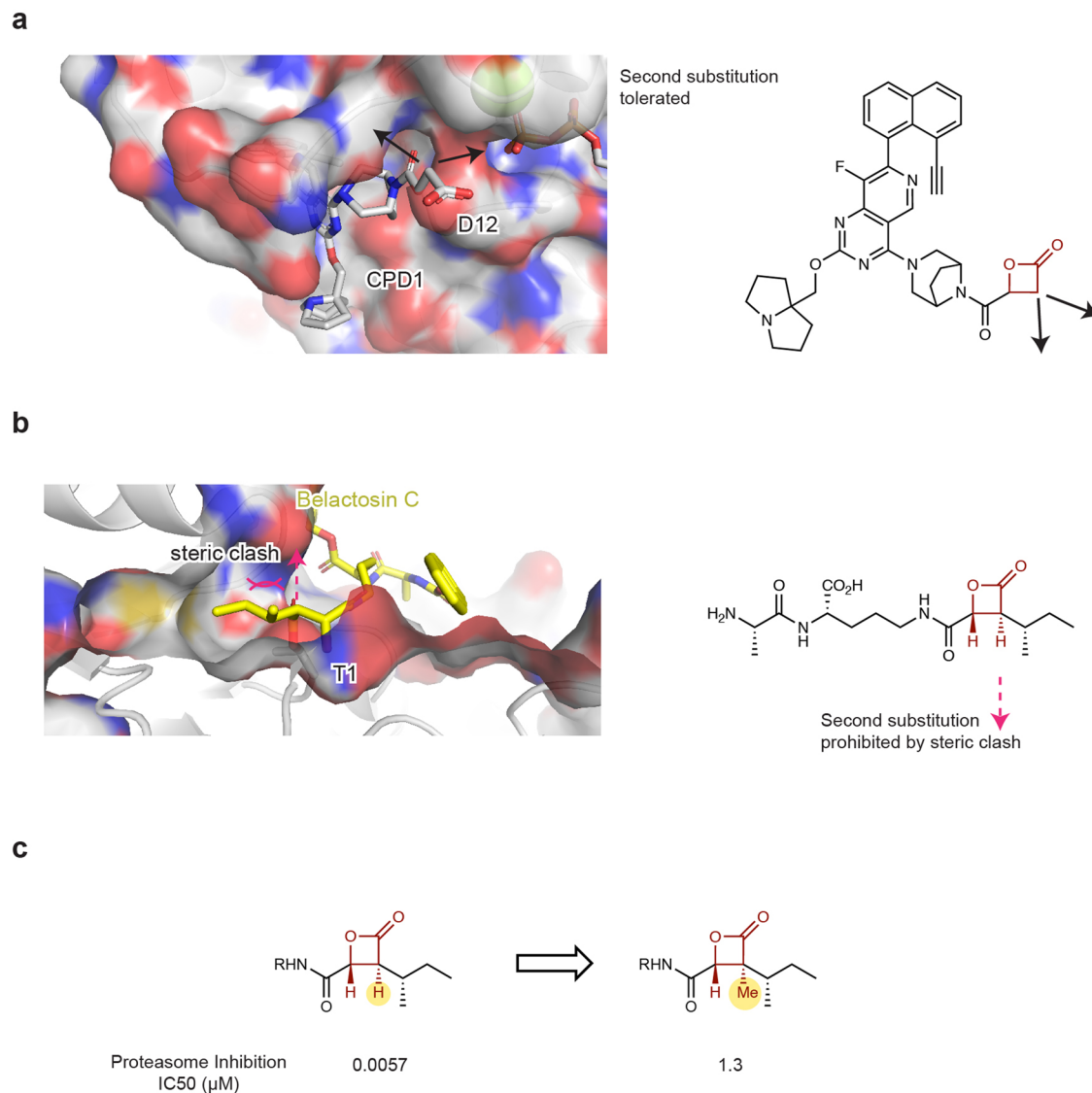




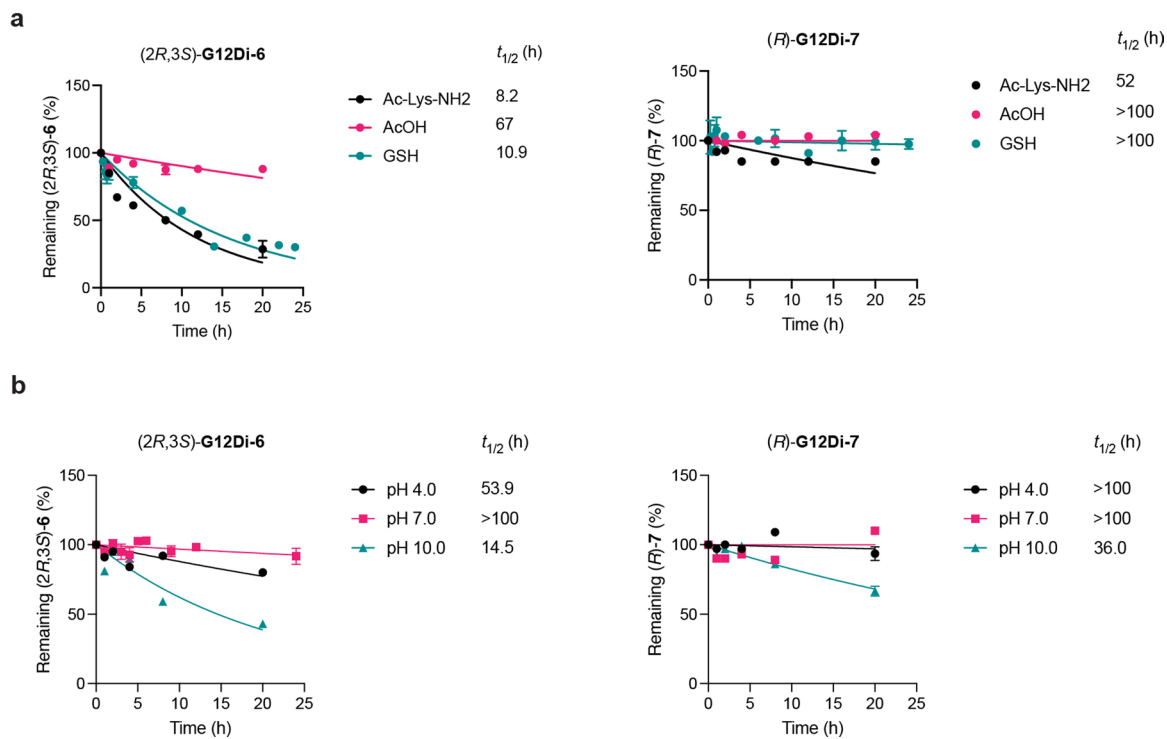
**Extended Data Fig. 5 | Cell growth inhibition of advanced  $\beta$ -lactone G12Di against a panel of G12D or non-G12D cell lines. a**, Cell growth inhibition curves. All data points represent individual biological replicates. Data are presented as mean  $\pm$  SD ( $n = 3$ ). **b**, Half-maximal inhibitory concentrations ( $IC_{50}$ s) of each biological replicate are plotted.



**Extended Data Fig. 6 | Malactone compounds 4–6 inhibited 20 S proteasome while (R)-7 did not. a**, Chemical structures of Compound 6 and Belactosin C with  $\beta$ -lactone warhead highlighted in red. **b**, Immunoblot of poly-ubiquitinated proteins in HEK293 cells. All data points represent individual biological replicates. Data are presented as mean  $\pm$  SD ( $n = 3$ ).

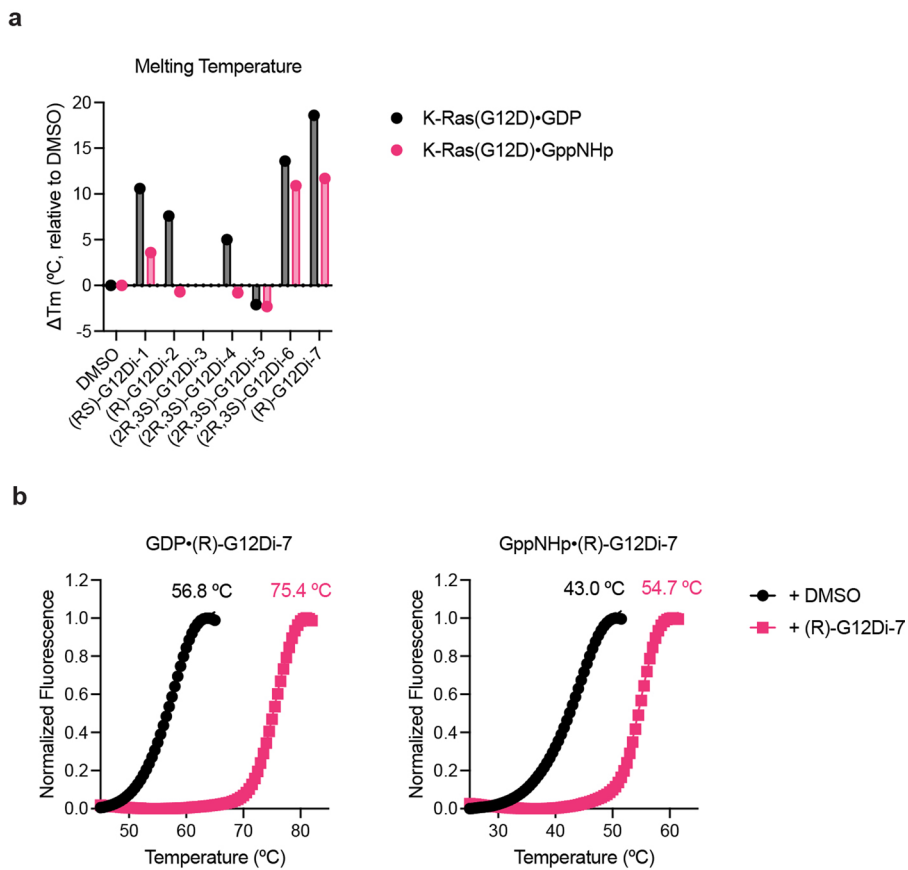


**Extended Data Fig. 7 | Analysis of X-ray co-crystal structures containing covalent malolactone electrophile. a,**  $\alpha$ -Carbon of malolactone G12Di could tolerate geminal disubstitution. **b,** Belactosin C could not tolerate a second  $\alpha$ -substitution. **c,** Additional methyl group (circled in yellow) in belactosin analog caused significant loss of activity.

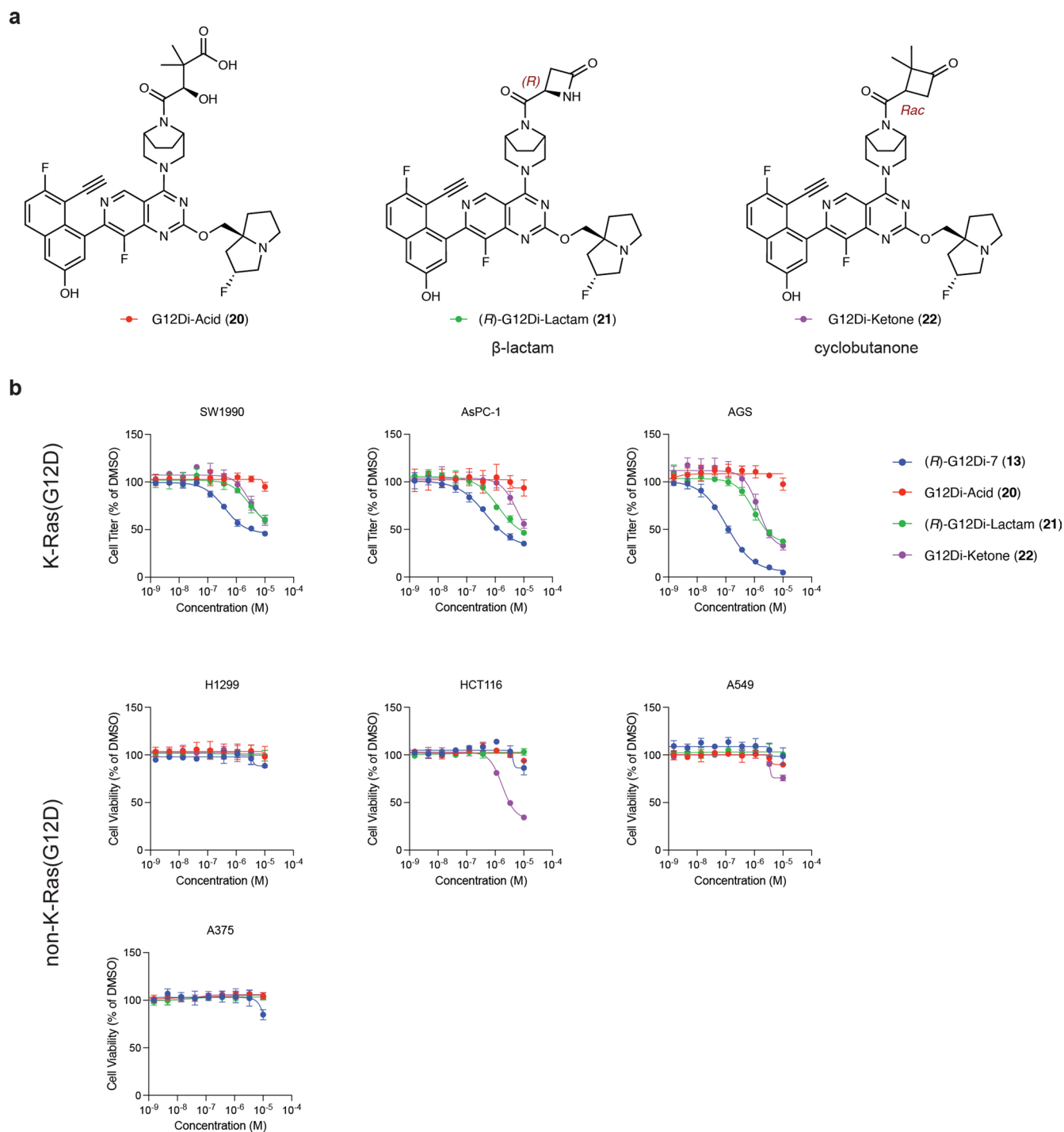


**Extended Data Fig. 8 | Intrinsic reactivity and stability of G12Di-6 and 7.**  
**a**, Stability in the presence of excess compounds (5 mM) bearing reactive functional groups. All data points represent individual biological replicates.

Data are presented as mean  $\pm$  SD ( $n = 2$ ). **b**, Stability in 1X PBS at various pH. All data points represent individual biological replicates. Data are presented as mean  $\pm$  SD ( $n = 2$ ).



**Extended Data Fig. 9 | Melting point change of covalently crosslinked K-Ras-G12D.** **a**, Summary of thermal stabilization of K-Ras-G12D by G12Di-1–7. **b**, DSF melting curves of K-Ras-G12D•GDP or GppNHp covalently bound to (R)-G12Di-7. All data points represent individual biological replicates. Data are presented as mean  $\pm$  SD ( $n = 3$ ).



**Extended Data Fig. 10 | Covalency of malolactone is important for the G12D cell growth inhibition.** **a**, Chemical structures of covalent K-Ras-G12D inhibitor and non-covalent analogs. **b**, Non-covalent analogs inhibited K-Ras-G12D cell lines with significantly lower potency. All data points represent individual biological replicates. Data are presented as mean  $\pm$  SD ( $n = 3$ ).

## Reporting Summary

Nature Portfolio wishes to improve the reproducibility of the work that we publish. This form provides structure for consistency and transparency in reporting. For further information on Nature Portfolio policies, see our [Editorial Policies](#) and the [Editorial Policy Checklist](#).

### Statistics

For all statistical analyses, confirm that the following items are present in the figure legend, table legend, main text, or Methods section.

n/a | Confirmed

- The exact sample size ( $n$ ) for each experimental group/condition, given as a discrete number and unit of measurement
- A statement on whether measurements were taken from distinct samples or whether the same sample was measured repeatedly
- The statistical test(s) used AND whether they are one- or two-sided  
*Only common tests should be described solely by name; describe more complex techniques in the Methods section.*
- A description of all covariates tested
- A description of any assumptions or corrections, such as tests of normality and adjustment for multiple comparisons
- A full description of the statistical parameters including central tendency (e.g. means) or other basic estimates (e.g. regression coefficient) AND variation (e.g. standard deviation) or associated estimates of uncertainty (e.g. confidence intervals)
- For null hypothesis testing, the test statistic (e.g.  $F$ ,  $t$ ,  $r$ ) with confidence intervals, effect sizes, degrees of freedom and  $P$  value noted  
*Give  $P$  values as exact values whenever suitable.*
- For Bayesian analysis, information on the choice of priors and Markov chain Monte Carlo settings
- For hierarchical and complex designs, identification of the appropriate level for tests and full reporting of outcomes
- Estimates of effect sizes (e.g. Cohen's  $d$ , Pearson's  $r$ ), indicating how they were calculated

*Our web collection on [statistics for biologists](#) contains articles on many of the points above.*

### Software and code

Policy information about [availability of computer code](#)

Data collection

Western Blot: LICOR Odyssey 2.1  
Plate Reader: TECAN SparkControl 2.1  
LC-MS: Waters MassLynx 4.2

Data analysis

GraphPad Prism 10.0.2  
MestReNova 14.2.0  
ImageJ 1.53k  
CCP4i2 1.0.2 (including iMosflm 7.4.0, Aimless 0.7.4, and Phaser 2.8.3 modules)  
Coot 0.9.6  
Phenix 1.19.2  
MaxQuant 2.0.3.1

For manuscripts utilizing custom algorithms or software that are central to the research but not yet described in published literature, software must be made available to editors and reviewers. We strongly encourage code deposition in a community repository (e.g. GitHub). See the Nature Portfolio [guidelines for submitting code & software](#) for further information.

## Data

Policy information about [availability of data](#)

All manuscripts must include a [data availability statement](#). This statement should provide the following information, where applicable:

- Accession codes, unique identifiers, or web links for publicly available datasets
- A description of any restrictions on data availability
- For clinical datasets or third party data, please ensure that the statement adheres to our [policy](#)

Atomic coordinates and structure factors for the reported crystal structures have been deposited with the Protein Data Bank (PDB), with the following accession numbers: K-Ras(G12D)•GDP•1, 8T4V.

Additional data used in this study are PDB 7PRZ, 6UTO, 6OIM.

Protein sequences used in this study are at Uniprot (<https://uniprot.org>) with the following accession codes P01116 (K-Ras, the 1-169 short form was used).

Source data of uncropped, unprocessed gel images are provide with this paper.

## Research involving human participants, their data, or biological material

Policy information about studies with [human participants or human data](#). See also policy information about [sex, gender \(identity/presentation\), and sexual orientation](#) and [race, ethnicity and racism](#).

Reporting on sex and gender	N/A
Reporting on race, ethnicity, or other socially relevant groupings	N/A
Population characteristics	N/A
Recruitment	N/A
Ethics oversight	N/A

Note that full information on the approval of the study protocol must also be provided in the manuscript.

## Field-specific reporting

Please select the one below that is the best fit for your research. If you are not sure, read the appropriate sections before making your selection.

- Life sciences       Behavioural & social sciences       Ecological, evolutionary & environmental sciences

For a reference copy of the document with all sections, see [nature.com/documents/nr-reporting-summary-flat.pdf](https://www.nature.com/documents/nr-reporting-summary-flat.pdf)

## Life sciences study design

All studies must disclose on these points even when the disclosure is negative.

Sample size	For plate reader based assays, three technical replicates were performed in each experiment. All experiments except crystallography have been performed in at least two biological replicates. See figure legends for exact number of biological replicates for each experiment. For mouse experiment, at least eight mice were used for each group. The determination of the sample size was based on achieving the minimum number of animals required for sacrifice while also ensuring statistical validity. The exact sample size was indicated in the figure legend.
Data exclusions	No data were excluded from analysis.
Replication	All attempts for replication were successful (see figure legends for the number of replicates for each experiment). We did not replicate X-ray crystallography experiment because of its nature.
Randomization	All mice xenografted with tumor were randomized in assigning to treatment and control groups. Besides mouse experiments, each biochemical experiment in this study is rationally designed and leads to a specific conclusion. Thus, samples were not randomized.
Blinding	Samples were not blinded. Each biochemical experiment in this study is rationally designed and leads to a specific conclusion.

## Reporting for specific materials, systems and methods



We require information from authors about some types of materials, experimental systems and methods used in many studies. Here, indicate whether each material, system or method listed is relevant to your study. If you are not sure if a list item applies to your research, read the appropriate section before selecting a response.

## Materials & experimental systems

n/a	Involved in the study
<input type="checkbox"/>	<input checked="" type="checkbox"/> Antibodies
<input type="checkbox"/>	<input checked="" type="checkbox"/> Eukaryotic cell lines
<input checked="" type="checkbox"/>	<input type="checkbox"/> Palaeontology and archaeology
<input type="checkbox"/>	<input checked="" type="checkbox"/> Animals and other organisms
<input checked="" type="checkbox"/>	<input type="checkbox"/> Clinical data
<input checked="" type="checkbox"/>	<input type="checkbox"/> Dual use research of concern
<input checked="" type="checkbox"/>	<input type="checkbox"/> Plants

## Methods

n/a	Involved in the study
<input checked="" type="checkbox"/>	<input type="checkbox"/> ChIP-seq
<input checked="" type="checkbox"/>	<input type="checkbox"/> Flow cytometry
<input checked="" type="checkbox"/>	<input type="checkbox"/> MRI-based neuroimaging

## Antibodies

### Antibodies used

Phospho-Akt (Ser473), Cell Signaling Technology, #4060, D9E  
 Akt, Cell Signaling Technology, #2920, 40D4  
 Phospho-p44/42 MAPK (Erk1/2) (Thr202/Tyr204), Cell Signaling Technology, #9101, Polyclonal  
 p44/42 MAPK (Erk1/2), Cell Signaling Technology, #4695, 137F5  
 Ras (G12D Mutant), Invitrogen, #MA5-36256, HL10  
 Ras, Abcam, #ab108602, EPR3255  
 GAPDH, ProteinTech, #60004-1-Ig, 1E6D9  
 Ubiquitin, Santa Cruz Biotechnology, #sc-8017, P4D1  
 β-Actin, Cell Signaling Technology, #8457, D6A8  
 goat anti-rabbit IgG-IRDye 800, LI-COR, 926-32211, Clone # Not Available  
 goat anti-mouse IgG-IRDye 680, LI-COR, 926-68070, Clone # Not Available

### Validation

All commercial antibodies have been validated by the manufacturers, see below:  
 Phospho-Akt (Ser473), <https://www.cellsignal.com/products/primary-antibodies/phospho-akt-ser473-d9e-xp-rabbit-mab/4060>  
 Akt, <https://www.cellsignal.com/products/primary-antibodies/akt-pan-40d4-mouse-mab/2920>  
 Phospho-p44/42 MAPK (Erk1/2) (Thr202/Tyr204), <https://www.cellsignal.com/products/primary-antibodies/phospho-p44-42-mapk-erk1-2-thr202-tyr204-antibody/9101>  
 p44/42 MAPK (Erk1/2), <https://www.cellsignal.com/products/primary-antibodies/p44-42-mapk-erk1-2-137f5-rabbit-mab/4695>  
 Ras (G12D Mutant), <https://www.thermofisher.com/antibody/product/Ras-G12D-Mutant-Antibody-clone-HL10-Monoclonal/MA5-36256>  
 Ras, <https://www.abcam.com/products/primary-antibodies/ras-antibody-epr3255-ab108602.html>  
 GAPDH, <https://www.ptglab.com/products/GAPDH-Antibody-60004-1-Ig.htm>  
 Ubiquitin, <https://www.scbt.com/p/ubiquitin-antibody-p4d1>  
 β-Actin, <https://www.cellsignal.com/products/primary-antibodies/b-actin-d6a8-rabbit-mab/8457>  
 goat anti-rabbit IgG-IRDye 800, [https://www.licor.com/bio/reagents/irdye-800cw-goat-anti-rabbit-igg-secondary-antibody?utm\\_source=google&utm\\_medium=adwords&utm\\_content=reagent-webpage&utm\\_campaign=reagents&gclid=Cj0KCQjwNgNanBhDUARIsAAelcAvn3g3GbfE8Gir0ag7cn1ZFmFjXBKe\\_\\_ip5ndT2hgRNNmCQV4IVSmcaAo6yEALw\\_wcB](https://www.licor.com/bio/reagents/irdye-800cw-goat-anti-rabbit-igg-secondary-antibody?utm_source=google&utm_medium=adwords&utm_content=reagent-webpage&utm_campaign=reagents&gclid=Cj0KCQjwNgNanBhDUARIsAAelcAvn3g3GbfE8Gir0ag7cn1ZFmFjXBKe__ip5ndT2hgRNNmCQV4IVSmcaAo6yEALw_wcB)  
 goat anti-mouse IgG-IRDye 680, [https://www.licor.com/bio/reagents/irdye-680rd-goat-anti-mouse-igg-secondary-antibody?utm\\_source=google&utm\\_medium=adwords&utm\\_content=reagent-webpage&utm\\_campaign=reagents&gclid=Cj0KCQjwNgNanBhDUARIsAAelcAt6VaxQsaaWaLsaFCTUplk4\\_RDD4Cy9KkbAJkn\\_wsSRPv7jAIky5m0aAr05EALw\\_wcB](https://www.licor.com/bio/reagents/irdye-680rd-goat-anti-mouse-igg-secondary-antibody?utm_source=google&utm_medium=adwords&utm_content=reagent-webpage&utm_campaign=reagents&gclid=Cj0KCQjwNgNanBhDUARIsAAelcAt6VaxQsaaWaLsaFCTUplk4_RDD4Cy9KkbAJkn_wsSRPv7jAIky5m0aAr05EALw_wcB)

## Eukaryotic cell lines

Policy information about [cell lines and Sex and Gender in Research](#)

### Cell line source(s)

SW1990: American Type Culture Collection (ATCC)  
 AsPC-1: American Type Culture Collection (ATCC)  
 AGS: American Type Culture Collection (ATCC)  
 H1299: American Type Culture Collection (ATCC)  
 HCT116: American Type Culture Collection (ATCC)  
 A549: American Type Culture Collection (ATCC)  
 A375: American Type Culture Collection (ATCC)  
 Ba/F3: German Collection of Microorganisms and Cell Cultures GmbH (DSMZ)  
 HEK293: American Type Culture Collection (ATCC)

### Authentication

Cell lines from ATCC and DSMZ were STR profiled by the manufacturer.

### Mycoplasma contamination

All cell lines were tested mycoplasma negative using MycoAlert™ Mycoplasma Detection Kit (Lonza).

### Commonly misidentified lines (See [ICLAC](#) register)

None

## Animals and other research organisms

Policy information about [studies involving animals](#); [ARRIVE guidelines](#) recommended for reporting animal research, and [Sex and Gender in Research](#)

Laboratory animals	6-9 week old, female, NOD/SCID mice. All animals were housed for a minimum 6-day stabilization period. Animals were observed daily for any clinical signs of disease. Animals were housed in individual HEPA ventilated cages (Innocage® IVC, Innovive USA). Fluorescent lighting was provided on a 12-hour cycle. Temperature and humidity were monitored and recorded daily and maintained to the maximum extent possible between 68-79°F (20-26°C) and 30-70% humidity, respectively. 2920X.10 18% soy irradiated rodent feed (Envigo) was provided and available ad libitum. Autoclaved acidified water (pH 2.5-3) was supplied ad libitum to all animals. Cage changes were performed every 2 weeks.
Wild animals	No wild animals were used.
Reporting on sex	Only female mice were used in these studies. Sex was not considered in study design in these experiments as the studies focus on cancer signaling.
Field-collected samples	Study did not involve samples collected from the field.
Ethics oversight	All animal studies were performed at Crown Bioscience (San Diego, CA). All the animal study procedures were performed in the SPF animal facility at Crown Bioscience under the approved protocols by the IACUC, with the guidance of the Association for Assessment and Accreditation of Laboratory Animal Care.

Note that full information on the approval of the study protocol must also be provided in the manuscript.

## Plants

Seed stocks	N/A
Novel plant genotypes	N/A
Authentication	N/A